Biophysical *Journal*
Article

Biophysical Society

Deciphering the mechanisms of HPV E6 mutations in the destabilization of E6/E6AP/p53 complex

Le Li,[1] Xuewei Dong,[1] Yiming Tang,[1] Zenghui Lao,[1] Xuhua Li,[2] Jiangtao Lei,[3] and Guanghong Wei[1,*]
[1]Department of Physics, State Key Laboratory of Surface Physics, and Key Laboratory for Computational Physical Sciences (Ministry of Education), Fudan University, Shanghai, China; [2]MOE Key Laboratory for Nonequilibrium Synthesis and Modulation of Condensed Matter, School of Physics, Xi'an Jiaotong University, Xi'an, China; and [3]Institute of Space Science and Technology, Nanchang University, Xuefu Avenue 999, Nanchang City, China

ABSTRACT In epithelial tumors, oncoprotein E6 binds with the ubiquitin ligase E6AP to form E6/E6AP heterodimer; then this heterodimer recruits p53 to form E6/E6AP/p53 heterotrimer and induces p53 degradation. Recent experiments demonstrated that three E6 single-site mutants (F47R, R102A, and L50E) can inhibit the E6/E6AP/p53 heterotrimer formation and rescue p53 from the degradation pathway. However, the molecular mechanism underlying mutation-induced heterotrimer inhibition remains largely elusive. Herein, we performed extensive molecular dynamics simulations (totally ~13 μs) on both heterodimer and heterotrimer to elucidate at an atomic level how each p53-degradation-defective HPV16 E6 mutant reduces the structural stabilities of the two complexes. Our simulations reveal that the three E6 mutations destabilize the structure of E6/E6AP/p53 complex through distinct mechanisms. Although $F47R^{E6}$ mutation has no effect on the structure of E6/E6AP heterodimer, it results in an electrostatic repulsion between $R47^{E6}$ and $R290^{p53}$, which is unfavorable for E6-p53 binding. $R102A^{E6}$ mutation destabilizes the structure of E6/E6AP heterodimer and significantly disrupts hydrophobic and cation-π interactions between $F47^{E6}$ and $E286^{p53}$/$L298^{p53}$/$R290^{p53}$. $L50E^{E6}$ mutation impairs both E6 interdomain interactions (especially F47-K108 cation-π interaction) and E6-E6AP intermolecular interactions important for the stabilization of E6/E6AP heterodimer. This study identifies the intra- and intermolecular interactions crucial for the complex stability, which may provide mechanistic insights into the inhibition of complex formation by the three HPV16 E6 mutations.

SIGNIFICANCE The most studied function of high-risk HPV E6 is the E6-ubiquitin-mediated degradation of tumor suppressor p53 by forming E6/E6AP/p53 heterotrimer. Recent experiments demonstrated that three E6 single-site mutants (F47R, R102A, and L50E) can inhibit the E6/E6AP/p53 heterotrimer formation and rescue p53 from the degradation pathway. The underlying molecular mechanism is yet poorly understood. Using all-atom molecular dynamics simulations, we investigate the mechanism of the three HPV16 E6 mutants (F47R, R102A, and L50E) in the destabilization of E6/E6AP and E6/E6AP/p53 complex and identify the molecular interactions (E6 interdomain interactions, E6-E6AP and E6-p53 intermolecular interactions) crucial for the formation of heterodimer/heterotrimer. Our results may provide possible target sites for disrupting the HPV16 E6-mediated p53 degradation.

INTRODUCTION

Tumor suppressor p53, as a "guardian of the genome" (1), regulates a series of gene expression patterns involved in cell cycle arrest, damaged DNA repair, and cell apoptosis in response to the cell stress (2). According to the International Agency for Research on Cancer (IARC) TP53 Database, more than 50% of human cancers are linked to the inactivation of p53 (3). In the normal cells, the level of p53 is stable via a negative feedback loop with oncoprotein MDM2 that degrades p53 by the ubiquitin-mediated protein degradation pathway (4). In response to cell stress, the MDM2-ubiquitin-mediated degradation of p53 is inhibited, and then the level of p53 increases in normal cells (5). However, the level of p53 in cervical carcinoma cells infected by high-risk human papillomaviruses (HPVs) is lower than that in normal cells because the product oncoprotein E6 of high-risk HPVs can degrade p53 via the ubiquitin-mediated degradation and decrease the level of p53 (6). More specifically, E6 is a viral oncoprotein of high-risk HPV. HPVs are double-stranded DNA viruses and have over 180 subtypes. Except for high-risk HPVs, low-risk HPVs also exist (7,8).

Submitted March 30, 2021, and accepted for publication March 28, 2022.
*Correspondence: ghwei@fudan.edu.cn
Editor: Diego U Ferreiro.
https://doi.org/10.1016/j.bpj.2022.03.030

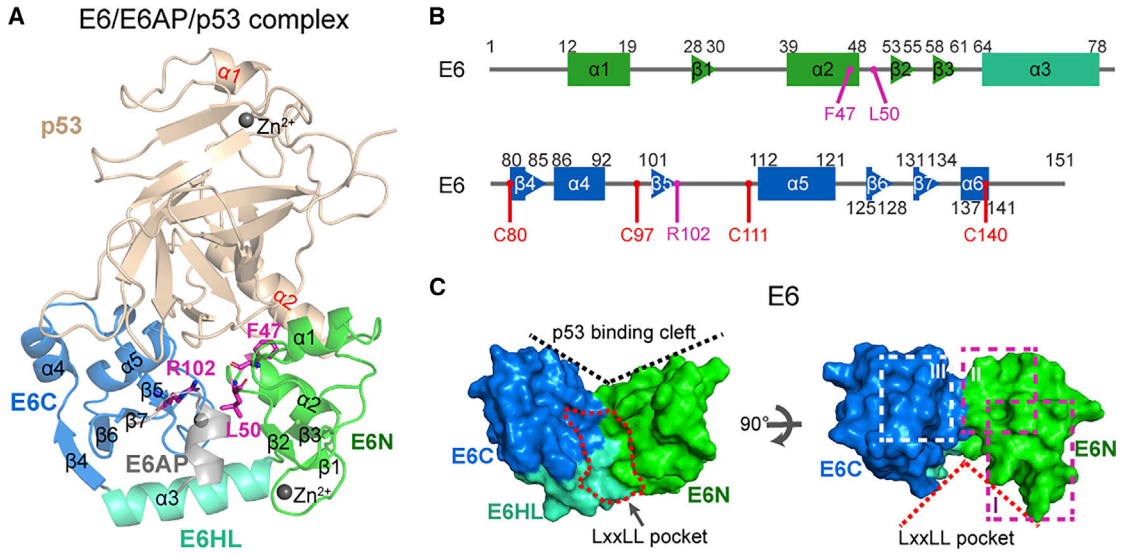

FIGURE 1 E6/E6AP/p53 heterotrimer in the x-ray crystal structure (PDB: 4XR8). (*A*) The cartoon representation of E6/E6AP/p53 heterotrimer. E6N and E6C: N- and C-terminal zinc-binding domains; E6HL: E6 helix linker. (*B*) The sequence of E6, where four C-to-S mutation sites and three p53-degradation-defective mutation sites (F47, L50, and R102) are labeled. (*C*) The surface representation of E6 with different views. E6 in the left panel of (*C*) is shown in the same view as that in (*A*). In (*A*)–(*C*), wheat: p53; green: E6N; cyan: E6HL; blue: E6C; gray: LxxLL motif of E6AP. To see figure in color, go online.

High-risk HPVs cause more than 90% of cervical carcinomas and 20% of head-neck squamous carcinomas (9,10), whereas low-risk HPVs are associated with benign cellular proliferations (11). HPV-16 and -18 are the most prevalent high-risk HPVs and they cause over 50% and 20% of cervical carcinomas respectively (12,13).

Earlier experimental studies reported the high-risk HPV E6-mediated p53 degradation pathway: E6 firstly binds to the acidic leucine-rich LxxLL motif of E6-association protein (E6AP) to form E6/E6AP heterodimer (14); subsequently, E6/E6AP heterodimer recruits p53 to form E6/E6AP/p53 heterotrimer, and then p53 is degraded through the ubiquitin-mediated protein degradation pathway (15). E6AP is an E3 ubiquitin ligase and is unable to degrade p53 when E6 is absent (16). E6 also targets other cellular proteins (17), such as interferon regulatory factor-3 (18), co-activators p300 and CREB binding protein (19), the human homolog of the *Drosophila* discs-large tumor suppressor protein (20), and the membrane-associated guanylate kinases (21,22). Therefore, oncoprotein E6 is a critical factor responsible for the cellular transformation and tumorigenesis (23).

The x-ray crystal structure of E6/E6AP/p53 heterotrimer (PDB: 4XR8) (Fig. 1 *A*) encoded by high-risk HPV-16 was resolved in 2016 (24) by Travé, Zanier, and their coworkers. This complex consists of full-length E6 (residues 1–151), the LxxLL motif ($_{372}$ELTLQELLGEER$_{383}$) of E6AP, and p53 core domain (p53C, residues 94–292). The full-length E6 contains two zinc-binding domains E6N (residues 1–61) and E6C (residues 79–151) that are linked by E6 helix linker (abbreviated E6HL, residues 62–78) (Figs. 1 *A* and *B*). In the crystal structure, the four cysteines (4C: C80, C97, C111, and C140) of E6 are mutated to four serines (4S) to prevent disulfide-mediated aggregation (Fig. 2 *B*) (24). It was reported that the efficiency of E6 4C/4S mutant to degrade p53 is almost equal to wild-type (WT) E6 (24). The LxxLL motif of E6AP is embedded in the hydrophobic cavity (also called LxxLL pocket) that is formed by E6N, E6C, and E6HL (Figs. 1 *A* and *C*). Fig. S1 *A* shows the dominant interactions between the LxxLL motif of E6AP and E6 (25). p53C binds to the E6 cleft that is formed by E6N and E6C (Figs. 1 *A* and *C*). This cleft is called the p53 binding cleft. The E6-p53C interface is divided into three subinterfaces (right panel of Fig. 1 *C*), and the E6-p53C interactions at the three interfaces are shown in Fig. S1 *B* (24).

Neither E6 nor E6AP is separately able to recruit p53 (14,26), revealing that the formation of E6/E6AP heterodimer is a prerequisite for p53 binding. Formation of E6/E6AP/p53 heterotrimer is required for high-risk HPV-mediated degradation of p53 (24). Therefore, the inhibition of formation of E6/E6AP/p53 complex is a potential strategy to impair the p53 degradation activity of E6. The LxxLL pocket and the p53 binding cleft of E6 are used as ideal targets for the screening of some peptides and small molecules (27–31). In addition, some E6 mutations at the p53 binding cleft of E6 (F47R) or the LxxLL pocket of E6 (R102A and L50E) exhibit the ability to impede the formation of E6/E6AP/p53 heterotrimer and to destroy the p53 degradation activity of E6 (24,25,32,33). F47R^{E6} mutation does not impair the binding of E6 with E6AP (33), and the x-ray crystal structure of E6^{F47R} in complex with the LxxLL motif of E6AP has been resolved (25). This mutation hinders the binding between E6^{F47R}/E6AP heterodimer and p53, blocks

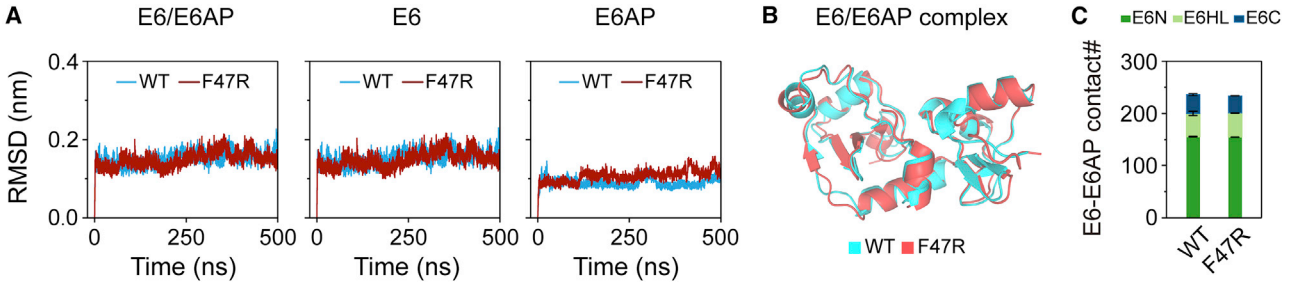

FIGURE 2 Analysis of structural stability of E6/E6AP and $E6^{F47R}$/E6AP heterodimers. (*A*) The time evolution of backbone RMSD values of E6/E6AP, E6, and E6AP relative to their initial conformations in WT and F47R mutant heterodimers. The RMSD values are averaged over three individual MD simulations. (*B*) The final structure of $E6^{F47R}$/E6AP heterodimer (pink) superposed with the final structure of WT E6/E6AP heterodimer (cyan). (*C*) Number of native contacts between E6 and E6AP in WT and F47R mutant heterodimers, residues 1–8 of E6 and 381–383 of E6AP. This result demonstrates that $F47R^{E6}$ mutation has no effect on the structure of E6/E6AP heterodimer. To see figure in color, go online.

the formation of E6/E6AP/p53 heterotrimer, and then rescues p53 from degradation pathway (24,32–34). $R102A^{E6}$ mutation located in the LxxLL pocket significantly reduces the binding affinity of E6 with E6AP and almost completely abolishes p53 degradation activity of E6 (25). Unlike $F47R^{E6}$ and $R102A^{E6}$ mutations, $L50E^{E6}$ mutation completely blocks the binding of E6AP-E6 and abolishes p53 degradation activity of E6 (25). Those experimental results demonstrate that the three single-site E6 mutations (F47R, R102A, and L50E) display different inhibitory effects on the formation of E6/E6AP heterodimer, but suggest that they all abolish the formation of E6/E6AP/p53 heterotrimer. In spite of extensive experimental studies and the emergence of computational studies on conformational dynamics of E6/E6AP heterodimer (29), the atomic-level mechanisms underlying the different inhibitory effects of the three E6 mutations on the bindings of E6-E6AP and E6/E6AP-p53 are poorly understood.

Molecular dynamics (MD) simulation is an effective technique in simulating biomolecule systems (35–37), and it has been widely used to investigate the conformational dynamics of p53C (38–41) and p53 isoforms (42), p53–DNA interaction (43), p53–MDM2 interaction (44,45), p53 peptide aggregation (46,47), and small molecule-p53C interaction (48). In this study, we utilized MD simulations to explore at the atomic level how the three individual mutations (F47R, R102A, and L50E) of E6 impede the stability of E6/E6AP/p53 complex. We performed three independent 500-ns MD simulations for each of the four heterodimers (WT E6/E6AP and the three E6/E6AP mutants) and three independent 800-ns MD simulations for each of the three heterotrimers (WT E6/E6AP/p53, $E6^{F47R}$/E6AP/p53, and $E6^{R102A}$/E6AP/p53). Here, E6AP refers to the LxxLL motif of E6AP. Our multiple MD simulations for the first time to our knowledge show how the three E6 mutations reduce the structural stabilities of the two complexes through different atomic-level mechanisms. This study may provide insights into the physical interactions crucial for the binding of E6-E6AP and E6-p53.

MATERIALS AND METHODS

Four E6/E6AP heterodimer systems: WT E6/E6AP, $E6^{F47R}$/E6AP, $E6^{R102A}$/E6AP, and $E6^{L50E}$/E6AP

The heterodimers of E6AP with WT E6 and three single-site E6 mutants (F47R, R102A, or L50E) are studied, and they are labeled as WT E6/E6AP, $E6^{F47R}$/E6AP, $E6^{R102A}$/E6AP, and $E6^{L50E}$/E6AP heterodimers. The initial coordinate of WT E6/E6AP heterodimer is taken from the x-ray crystal structure (PDB: 4XR8 (24), the LxxLL motif of E6AP (chain A): residues 372–383, E6 (chain F): residues 1–143). The three heterodimers with E6 mutants are generated by mutating the residues at the corresponding sites of WT E6 in E6/E6AP heterodimer using Pymol (49).

Three E6/E6AP/p53 heterotrimer systems: WT E6/E6AP/p53, $E6^{F47R}$/E6AP/p53, and $E6^{R102A}$/E6AP/p53

Three heterodimer systems are studied, including WT E6/E6AP/p53, $E6^{F47R}$/E6AP/p53, and $E6^{R102A}$/E6AP/p53 heterotrimers. The initial coordinate of WT E6/E6AP/p53 heterotrimer is taken from the x-ray crystal structure (PDB: 4XR8 (24), the LxxLL motif of E6AP (chain A): residues 372–383, p53C (chain C): residues 94–292, E6 (chain F): residues 1–143). $E6^{F47R}$/E6AP/p53 and $E6^{R102A}$/E6AP/p53 heterotrimers are obtained using the same strategy as that for the heterodimers with E6 mutants.

To mimic the neutral experimental pH condition (24) (~pH 7.0), in both heterodimers and heterotrimers, the side chains of Lys and Arg are protonated (Arg^+ and Lys^+), and the side chains of Glu and Asp are deprotonated (Glu^- and Asp^-). We predicted the residue pKa values of WT heterotrimer using Propka web server. The predicted result shows that all pKa values of His resides are less than pH 7.0, indicating that the total net charge of His residues is zero (i.e., in HID or HIE state). As ND atom of $His179^{p53}$ is coordinated to Zn^{2+}, this $His179^{p53}$ was modeled as the HIE tautomer. For simplicity, we modeled all His residues as the HIE tautomer. Using this His tautomeric state, our simulations show that both WT dimer and trimer remain stable during the full period of three replicate MD runs, in good agreement with experimental results (25). The agreement between our simulations and the experiments established the suitability of the HIE tautomeric state of HIS modeling in our simulations, so we modeled all His residues as HIE tautomer for all three mutants.

Simulation details

We carried out three independent 500-ns MD simulations for each E6/E6AP heterodimer system and three independent 800-ns MD simulations for each E6/E6AP/p53 heterotrimer system at 310 K using GROMACS 5.1.4 software package (50) in combination with CHARMM36m force field (51). Each

system is placed in a cubic box filled with TIP3P water, with a minimum distance of 1.2 nm between protein atoms and the box edges. Counterions (Cl^- ions) were added to neutralize the charge of each system. As done in our recent study (41), the distances of Zn^{2+} ion with the four coordinated atoms are restrained using the piecewise harmonic/linear potential energy, where a flat bottom potential is used when the distances between Zn^{2+} ion and four coordinated atoms are within a reference distance of 0.2 nm. The force constants are adopted from the work by Luo et al. (52), and the partial charges of atoms in the four coordinated residues are taken from CHARMM36m force field (51). In each system, solvent molecules were energy-minimized by steepest descent method for 10,000 steps with position restraints on the proteins. The solvent minimization was followed by another energy-minimization for 20,000 steps without position restraints on the proteins. Subsequently, each system was equilibrated under a canonical ensemble (T = 310 K) and followed by an isothermal-isobaric ensemble (T = 310 K, p = 1 bar), both for 0.1 ns. During canonical ensemble and isothermal-isobaric ensemble equilibrations, all-bonds of proteins were constrained using LINCS method, and no restraints were applied for protein heavy atoms. After that, 500-ns and 800-ns production MD simulations were performed under an isothermal-isobaric ensemble. The pressure was kept at 1 bar using Parrinello-Rahman method (53). The temperature was maintained at 310 K by separately coupling the protein and nonprotein groups to an external heat bath with velocity rescaling method (54). Electrostatic interactions were calculated using the particle mesh Ewald method with a real space cutoff of 1.4 nm (55). The van der Waals interactions were treated using a cutoff of 1.4 nm.

RESULTS AND DISCUSSION

$F47R^{E6}$ mutation leads to an electrostatic repulsion between $R47^{E6}$ and $R290^{p53}$, which disfavors the residue-residue interactions crucial for the stabilization of E6-p53 subinterface II and III.

The x-ray crystal structure of $E6^{F47R}$/E6AP heterodimer (PDB: 4DIZ) was resolved by Zanier et al. (25), and it is superimposable with the x-ray crystal structure of WT E6/E6AP heterodimer in E6/E6AP/p53 heterotrimer (PDB: 4XR8) (with a backbone RMSD of 0.12 nm), except for residues 1–8 of E6 and 381–383 of E6AP (24). This result demonstrates that $F47R^{E6}$ mutation has no effect on the structure of E6/E6AP heterodimer. In order to check whether CHARMM36m force field is suitable for our simulated systems, we first calculate the backbone RMSD values of E6/E6AP, E6, and E6AP averaged over the three MD runs for WT E6/E6AP or $E6^{F47R}$/E6AP heterodimer relative to their initial conformations. The average RMSD values of E6/E6AP, E6, and E6AP in $E6^{F47R}$/E6AP and WT E6/E6AP heterodimers are quite small (~0.2 nm) (Fig. 2 *A*). Quantitatively similar results are observed in each simulation (Fig. S2). These data indicate that the structure of $E6^{F47R}$/E6AP heterodimer is stable and highly similar to that of WT E6/E6AP heterodimer, which can also be clearly seen from the all-atom superposition of their final conformations (Fig. 2 *B*). The agreement between our simulations and the experiments established the suitability of CHARMM36m force field for E6/E6AP heterodimers. Moreover, we calculated the number of native contacts between E6 and E6AP in WT E6/E6AP and $E6^{F47R}$/E6AP heterodimers (Fig. 2 *C*), and the number of E6-E6AP in $E6^{F47R}$/E6AP heterodimer (234 ± 1) is almost the same as that in WT E6/E6AP heterodimer (236 ± 4). The average E6-E6AP binding energy over the three MD runs for $F47R^{E6}$ heterodimer (−55.55 kcal mol^{-1}) is similar to that for WT heterodimer (−55.81 kcal mol^{-1}) (Table S1), which further supports the results of E6-E6AP contact number analyses. Taken together, the contact number and binding free energy analyses are in good agreement with previous biophysical experiments, showing that $F47R^{E6}$ mutation has a negligible effect on the binding of E6 with E6AP (32).

Having now established the suitability of CHARMM36m force field for E6/E6AP heterodimer and p53 (41), we turn to the exploration of the effects of $F47R^{E6}$ mutation on interactions between E6/E6AP and p53, using the same protein force field. The RMSD values of E6/E6AP (Fig. S3 *A*) and native contact number of E6-E6AP (Fig. S3 *B*) in WT E6/E6AP/p53 heterotrimer are also similar to those in $E6^{F47R}$/E6AP/p53 heterotrimer, indicating that E6/E6AP in both WT and $F47R^{E6}$ heterotrimers is stable, and $F47R^{E6}$ mutation does not affect the structural stability of E6/E6AP in heterotrimer. However, the number of native contacts between p53 and $E6^{F47R}$/E6AP heterodimer is significantly decreased (Fig. 3 *A*), implying that $F47R^{E6}$ mutation disrupts the interactions between p53 and the heterodimer. Our simulation result is in a way consistent with recent experiments showing that $F47R^{E6}$ mutation can inhibit the association of p53 with E6/E6AP heterodimer (24,32,33). By calculating the number of native contacts of intermolecular residue pairs at E6-p53 subinterface, we find that $F47R^{E6}$ mutation weakens the residue-residue interactions crucial for the stabilization of E6-p53 subinterface II and III (Fig. 3 *B*). Almost all E6-p53 residue pairs at subinterface II display reduced interactions, including $Y43^{E6}$-$L289^{p53}$/$R290^{p53}$, $D44^{E6}$-$R290^{p53}$, $F47^{E6}$-$E286^{p53}$/$L289^{p53}$/$R290^{p53}$/$A129^{p53}$, and $D49^{E6}$-$P128^{p53}$. Specifically, $F47^{E6}$ in WT heterotrimer interacts with $R290^{p53}$ by a cation-π interaction (Figs. 3 *C* and S4), whereas this cation-π interaction in the mutant heterotrimer is destroyed. Moreover, $F47R^{E6}$ mutation results in an electrostatic repulsion between $R47^{E6}$ and $R290^{p53}$ (Fig. S4), which reduces the interactions of several residue pairs around $R47^{E6}$ and $R290^{p53}$, including hydrophobic interactions of $F47^{E6}$-$E286^{p53}$/$L289^{p53}$/$A129^{p53}$, $Y43^{E6}$-$L289^{p53}$, and $D49^{E6}$-$P128^{p53}$ (Fig. S4), $Y43^{E6}$-$R290^{p53}$ cation-π interaction (Figs. 3 *D* and S4), and $D44^{E6}$-$R290^{p53}$ salt bridge interaction (Figs. 3 *E* and S4). It is conceivable that these weakened intermolecular residue-residue interactions are crucial for the stability of the complex. Thus, we can reasonably infer that these interactions may be also important for the dimer/trimer formation. Our inference is supported by a recent study showing that a small-molecule inhibitor of E6-p53 interaction, identified by a structure-based virtual screening method using a druggable pseudocavity around $F47^{E6}$ and $D49^{E6}$, can reactivate p53 functions.

As residues at subinterface II are mostly located within α2-helix of E6 (residues 39–48) and α2-helix of p53 (residues 278–290) (Fig. S4). $F47R^{E6}$ mutation causes markedly increased distance between the two helixes (Figs. 3 *F* and

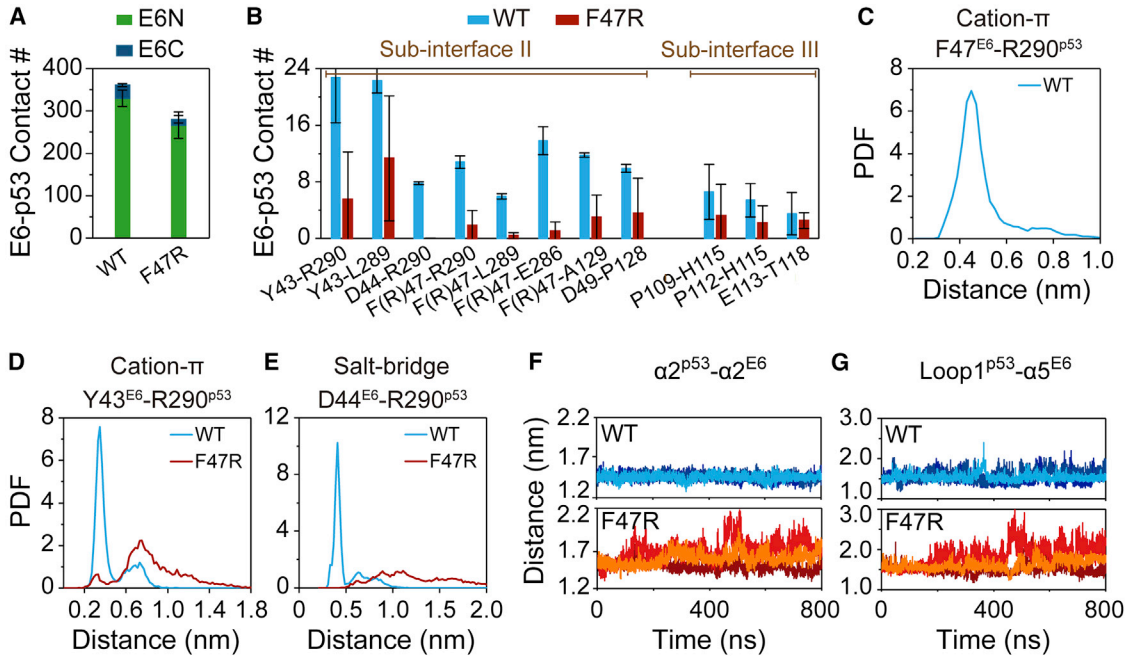

FIGURE 3 The effect of F47R^{E6} mutation on the interactions between E6 and p53 in E6/E6AP/p53 heterotrimer. (*A*) Native contact number of E6-p53 in WT E6/E6AP/p53 and E6^{F47R}/E6AP/p53 heterotrimers. (*B*) Native contact number of residue pairs at E6-p53 subinterface. Probability density function (PDF) of the minimum centroid distance between the ring of aromatic residues and ε-amino group (NH_3^+) in the side chain of Arg: (*C*) for F47^{E6}-R290^{p53} and (*D*) for Y43^{E6}-R290^{p53}. (*E*) PDF of the distance between the side chain charge center of D44^{E6} and R290^{p53}. (*F* and *G*) The time evolution of centroid distance (*F*) between α2-helix^{p53} and α2-helix^{E6} and (*G*) between loop1^{p53} and α5-helix^{E6}. To see figure in color, go online.

S4), indicating that α2-helix^{p53} tends to dissociate from E6^{F47R}/E6AP heterodimer. Due to the positive correlation between residues 278–282 within α2-helix^{p53} and residues 122–124 within loop1^{p53} (Fig. S5) in E6^{F47R}/E6AP/p53 heterotrimer, loop1^{p53} also tends to dissociate from E6^{F47R}/E6AP heterodimer (Figs. 3 *G* and S4), leading to reduced interactions at E6-p53 subinterface III (Fig. S4). Those decreased interactions include P109^{E6}/P112^{E6}-H115^{p53} hydrophobic interactions and E113^{E6}-T118^{p53} H-bonding interaction (Fig. S4). The H-bond occupancy between E113^{E6} and T118^{p53} is 21% in WT heterotrimer, and it is 11% in mutant heterotrimer (an average of three MD runs). As shown in Table S2, the MM/GBSA binding energy between E6 and p53 in F47R^{E6} (−29.31 kcal mol^{-1}) (Table S2) heterotrimer is higher than that in WT heterotrimer (−43.13 kcal mol^{-1}), which further supports the results of E6-p53 contact number analyses. These data indicate that when F47 is mutated into positively charged residue (R), the electrostatic repulsion between R47^{E6} and R290^{p53} would block the residue-residue interactions at E6-p53 subinterfaces and the formation of the heterotrimer.

R102A^{E6} mutation disrupts the hydrophobic and cation-π interactions between F47 of E6 and E286/L298/R290 of p53, crucial for the stabilization of heterotrimer

A pull-down experiment showed that R102A E6 mutant has a reduced binding ability with E6AP relative to WT E6 (25), indicating that E6^{R102A}/E6AP heterodimer is less stable than WT E6/E6AP heterodimer. To elucidate at an atomic level how R102A^{E6} mutation decreases the E6AP-binding ability of E6 or the structural stability of the heterodimer, we first calculated the time evolution of backbone RMSD values of WT E6/E6AP and E6^{R102A}/E6AP heterodimers (left panel in Fig. 4 *A*). It can be seen that R102A mutant heterodimer has a larger RMSD value than WT heterodimer (Figs. 4 *A* and S6), indicating that R102A^{E6} mutation decreases the structural stability of E6/E6AP heterodimer, in accordance with the pull-down experiments (25). In addition, R102A^{E6} mutation also destabilizes the structures of both E6 and E6AP (middle and right panels in Figs. 4 *A* and S6). We then analyzed the influence of R102A^{E6} mutation on the intramolecular residue-residue interactions crucial for the stabilization of E6. In WT E6, the side chain of R102^{E6C} forms H-bonds with the main chains of two residues R48^{E6N}/D49^{E6N} (22% and 32% H-bond occupancy, respectively) (Figs. 4 *B* and S7), thus holding E6C and E6N together and stabilizing the structure of E6. However, R102A^{E6} mutation abolishes the H-bonding interactions (Fig. S7) and destabilizes E6.

The number of native contacts between E6 and E6AP in E6^{R102A}/E6AP heterodimer (225 ± 3) is also smaller than that in WT E6/E6AP heterodimer (236 ± 4) (Fig. 4 *C*). Although the average E6-E6AP binding energy for R102A^{E6} dimer (−56.95 kcal mol^{-1}) is slightly lower than that for WT heterodimer (−55.81 kcal mol^{-1}) (Table S3),

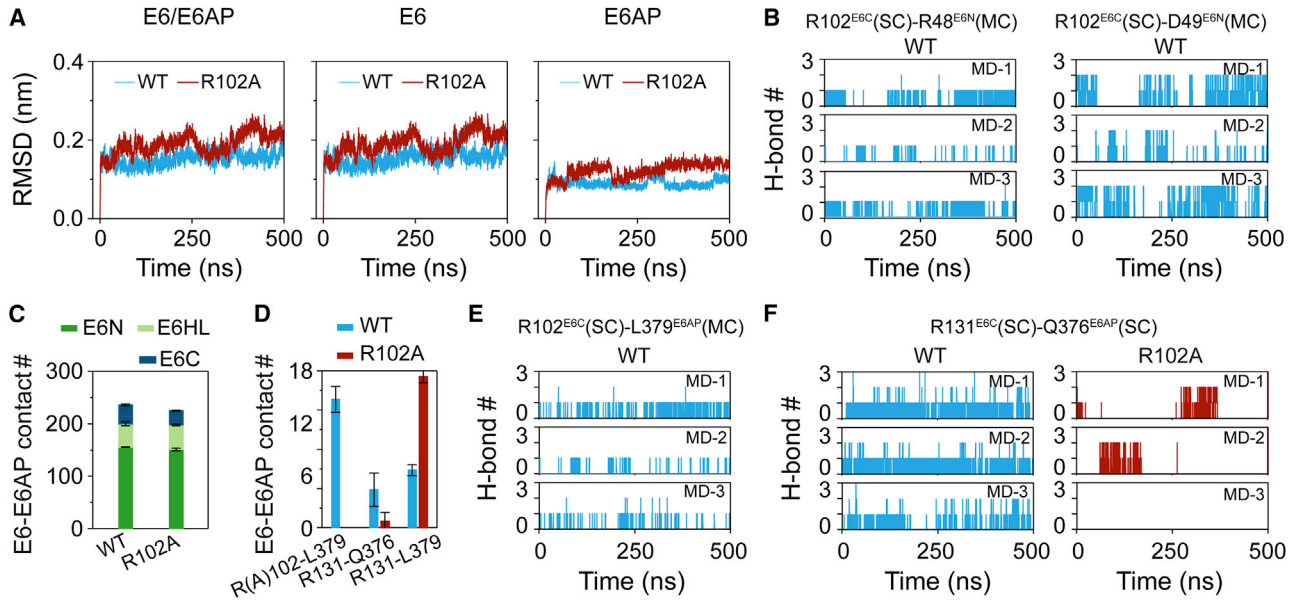

FIGURE 4 The influences of R102A^{E6} mutation on E6/E6AP heterodimer structure and crucial interactions stabilizing the heterodimer. (*A*) The time evolution of backbone RMSD values of E6/E6AP, E6, and E6AP relative to their initial conformations. The RMSD value is averaged over three individual MD simulations. (*B*) The time evolution of H-bond number between the side chain (SC) of R102^{E6} and the main chain (MC) of R48^{E6}/D49^{E6} in WT heterodimer. (*C*) Number of native contacts between E6 and E6AP. (*D*) Contact number of R(A)102^{E6}-L379^{E6AP}, R131^{E6}-Q376^{E6AP}, and R131^{E6}-L379^{E6AP}. (*E*) The time evolution of H-bond number between the SC of R102^{E6} and the MC of L379^{E6AP} in WT heterodimer. (*F*) The time evolution of H-bond number between the SCs of R131^{E6} and Q376^{E6AP}. To see figure in color, go online.

the E6-E6AP binding energy for R102A^{E6} dimer in two out of the three MD runs (−54.01 and −53.69 kcal mol^{-1}) is higher than that for WT dimer (−55.81 kcal mol^{-1}) (Table S4). The result is somehow consistent with the pull-down experiment showing that R102A^{E6} mutation led to an E6-E6AP binding probability of ∼25% relative to 100% of WT (inferred from Fig. 3 *B* in ref. 25). The decrease of E6-E6AP contact number is mostly contributed by two residue pairs between E6C and E6AP: R102^{E6C}-L379^{E6AP} and R131^{E6C}-Q376^{E6AP} (Fig. 4 *D*). An H-bond is formed between the side chain of R102^{E6} and the main chain of L379^{E6AP} (with an 8% H-bond occupancy) (Figs. 4 *D*, *E* and S7), whereas R102A^{E6} mutation eliminates the H-bond formation. R131^{E6} that is close to R102^{E6} (Fig. S7) has hydrophobic interaction with L379^{E6AP} (25). R102A mutation provides more space for the side chain of R131 (Fig. S7), thus facilitates the hydrophobic interaction between R131^{E6} and L379^{E6AP} (Figs. 4 *D* and S7), but it abolishes R131^{E6}-Q376^{E6AP} H-bonding interaction (Figs. 4 *D*, *F* and S7). The H-bond occupancies of R131^{E6}-Q376^{E6AP} in WT and R102A^{E6} heterotrimers are 35% and 0, respectively. These results suggest that R102A^{E6} mutation has minor influence on the interactions between E6N/E6HL and E6AP, and it eliminates the H-bond formation of E6C-E6AP residue pairs (R(A)102^{E6C}-L379^{E6AP}, R131^{E6C}-Q376^{E6AP}), thus destabilizing the structure of E6/E6AP heterodimer.

The p53 degradation assay experiments demonstrated that R102A^{E6} mutation abolishes p53 degradation (25), implying that R102A^{E6} mutation impedes the formation of E6/E6AP/p53 heterotrimer. In order to get some insights into the molecular mechanism by which R102A^{E6} mutation inhibits the formation of stable E6/E6AP/p53 heterotrimer, we first calculated the number of native contacts between E6 and p53 in WT and mutant heterotrimers. Fig. 5 *A* shows that R102A^{E6} mutation causes a decrease in the native contact number of E6-p53, revealing a disruptive effect of R102A^{E6} mutation on the interactions between E6 and p53. Further residue-based E6-p53 interaction analysis shows that R102A^{E6} mutation reduces the contact number of F47^{E6N}-E286^{p53}/L289^{p53}/R290^{p53} residue pairs (Fig. 5 *B*). F47^{E6N} interacts with E286^{p53}/L289^{p53} by hydrophobic interaction and with R290^{p53} by cation-π interaction in WT heterotrimer (24), whereas these interactions are greatly reduced in R102A^{E6} mutant heterotrimer (Figs. 5 *B*, *C* and *D*). The E6-p53 binding energy in R102A^{E6} heterotrimer (−40.17 kcal mol^{-1}) is higher than that in WT heterotrimer (−43.13 kcal mol^{-1}), which is consistent with the results of the contact number analysis.

To elucidate how R102A^{E6C} mutation results in a reduction in the interactions of those E6-p53 residue pairs, we calculated the side chain contact number of residue pairs within E6 in the two heterotrimers and find that R102A^{E6} mutation destroys R102^{E6C}-P109^{E6C} hydrophobic interaction (Figs. 5 *D* and *E*), which facilitates P109^{E6C}-K108^{E6C} H-bonding interaction (Figs. 5 *D*, *E* and *F*). The occupancies of P109^{E6C}-K108^{E6C} H-bond in WT and R102A^{E6} heterotrimers are 3% and 14%, respectively. This enhanced H-bonding interaction restrains the flexibility of the side

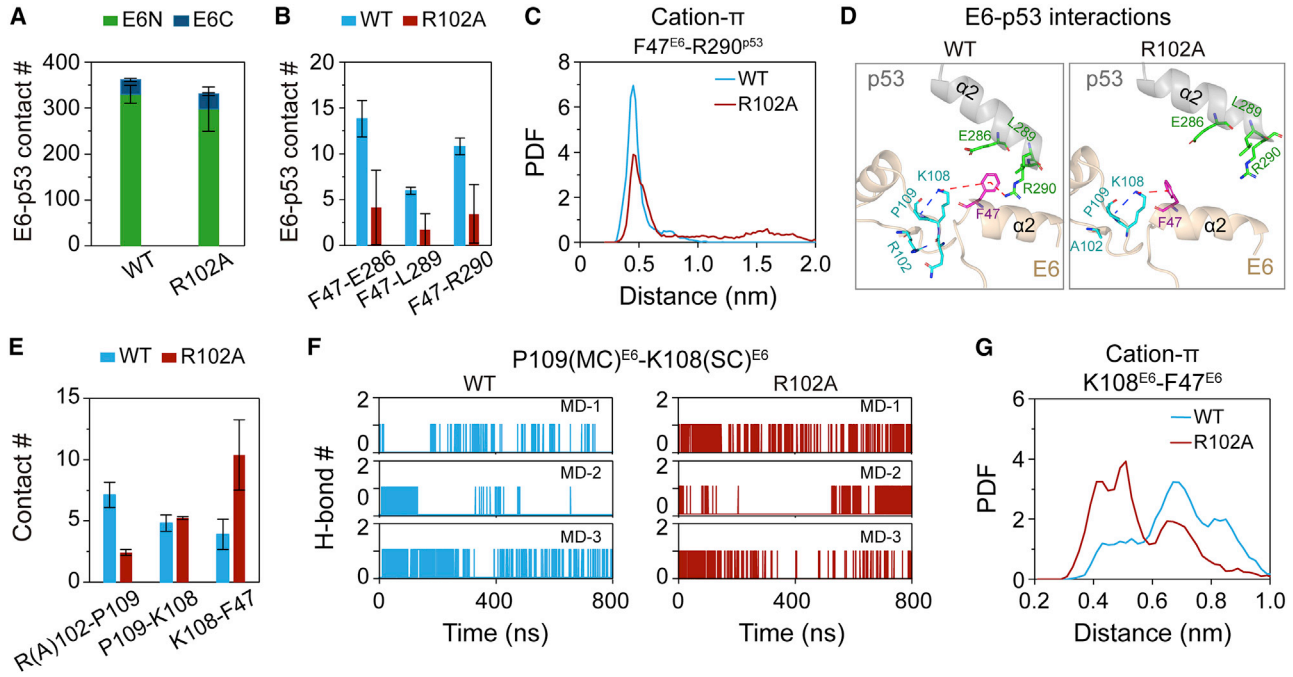

FIGURE 5 Mechanistic analyses of the inhibitory effect of $R102^{E6}$ mutation on the binding of p53 with E6/E6AP heterodimer. (*A*) Native contact number of E6-p53 in heterotrimers. (*B*) Number of contacts between $F47^{E6}$ and $E286^{p53}$/$L289^{p53}$/$R290^{p53}$. (*C*) Probability density function (PDF) of the minimum centroid distance between aromatic ring of $F47^{E6}$ and ε-amino group (NH_3^+) in the side chain of $R290^{p53}$. (*D*) The snapshots (the center structure of the first cluster obtained by clustering analysis) showing the $R102A^{E6}$ mutation-induced alteration of E6C-E6N and E6N-p53 interaction network. Thin red dashed line: cation-π interaction; thick blue dashed line: H-bond. (*E*) Side chain contact number of residue pairs: $R(A)102^{E6C}$-$P109^{E6C}$, $P109^{E6C}$-$K108^{E6C}$, and $K108^{E6C}$-$F47^{E6N}$. (*F*) The time evolution of H-bond number between the side chain (SC) of $K108^{E6}$ and the main chain (MC) of $P109^{E6}$ in WT and R102A mutant heterotrimers. (*G*) PDF of the centroid distance between the ring of aromatic residues $F47^{E6N}$ and ε-amino group (NH_3^+) in the side chain of $K108^{E6C}$. To see figure in color, go online.

chain of $K108^{E6C}$, which facilitates the $K108^{E6C}$-$F47^{E6N}$ cation-π interaction (Figs. 5 *D*, *E* and *G*), and in turn leads to a decrease in the aforementioned interactions ($F47^{E6N}$-$E286^{p53}$/$L298^{p53}$/$R290^{p53}$) between E6 and p53. Taken together, $R102A^{E6}$ mutation markedly disrupts the hydrophobic and cation-π interactions between F47 of E6 and E286/L298/R290 of p53, which may disfavor the binding of p53 with E6/E6AP heterodimer.

$L50E^{E6}$ mutation disrupts E6 interdomain hydrophobic, salt bridge, and cation-π interactions and E6-E6AP intermolecular hydrophobic interactions, thus destabilizes the structure of E6/E6AP heterodimer

In the pull-down experiments, $L50E^{E6}$ mutation completely suppresses the assembly of E6/E6AP complex and thus abolishes the p53 degradation activity of E6 (25). To understand how $L50E^{E6}$ mutation impedes the formation of E6/E6AP heterodimer, we first examined the effect of $L50E^{E6}$ mutation on the structural stability of $E6^{L50E}$/E6AP heterodimer by calculating the backbone RMSD values of E6/E6AP. It can be seen from Figs. 6 *A* and S8 that $E6^{L50E}$/E6AP heterodimer has a much larger RMSD value than WT E6/E6AP heterodimer, indicating that $L50E^{E6}$ mutation significantly disrupts the structure of E6/E6AP heterodimer. Both E6 and E6AP also display increased RMSD values (Figs. 6 *A* and S8), especially E6. We then explore how $L50E^{E6}$ mutation damages the structure of E6 by calculating the native contact number within E6 in WT E6/E6AP and $E6^{L50E}$/E6AP heterodimers (Fig. 6 *B*). The residue pairs stabilizing the E6N-E6HL and E6N-E6C interdomain interactions display distinctly decreased contact number (Fig. 6 *B*). At E6N-E6HL interface, the residue pairs with decreased interactions include $F45^{E6N}$-$V62^{E6HL}$, $L50^{E6N}$-$L67^{E6HL}$, and $R48^{E6N}$-$D64^{E6HL}$. $L50E^{E6}$ mutation almost completely disrupts $L50^{E6N}$-$L67^{E6HL}$ hydrophobic interaction and simultaneously leads to an electrostatic repulsion between $E50^{E6N}$ and $D64^{E6HL}$, which in turn results in the disappearance of $R48^{E6N}$-$D64^{E6HL}$ salt bridge and the reduction of $F45^{E6N}$-$V62^{E6HL}$ hydrophobic interaction (Figs. 6 *C* and *E*). At E6N-E6C interface, three residue pairs exhibit decreased interactions. Specifically, $F47^{E6N}$-$K108^{E6C}$ cation-π interaction (Figs. 6 *D* and *E*) is abolished, and hydrophobic interactions between the aliphatic groups of $R48^{E6N}$ and $C106^{E6C}$/$K108^{E6C}$ (Fig. 6 *E*) are significantly reduced. The marked decrease of E6N-E6HL and E6N-E6C interdomain interactions destabilize the structure of E6, especially E6C and E6HL regions (Fig. S9). The structural disruption of E6C and

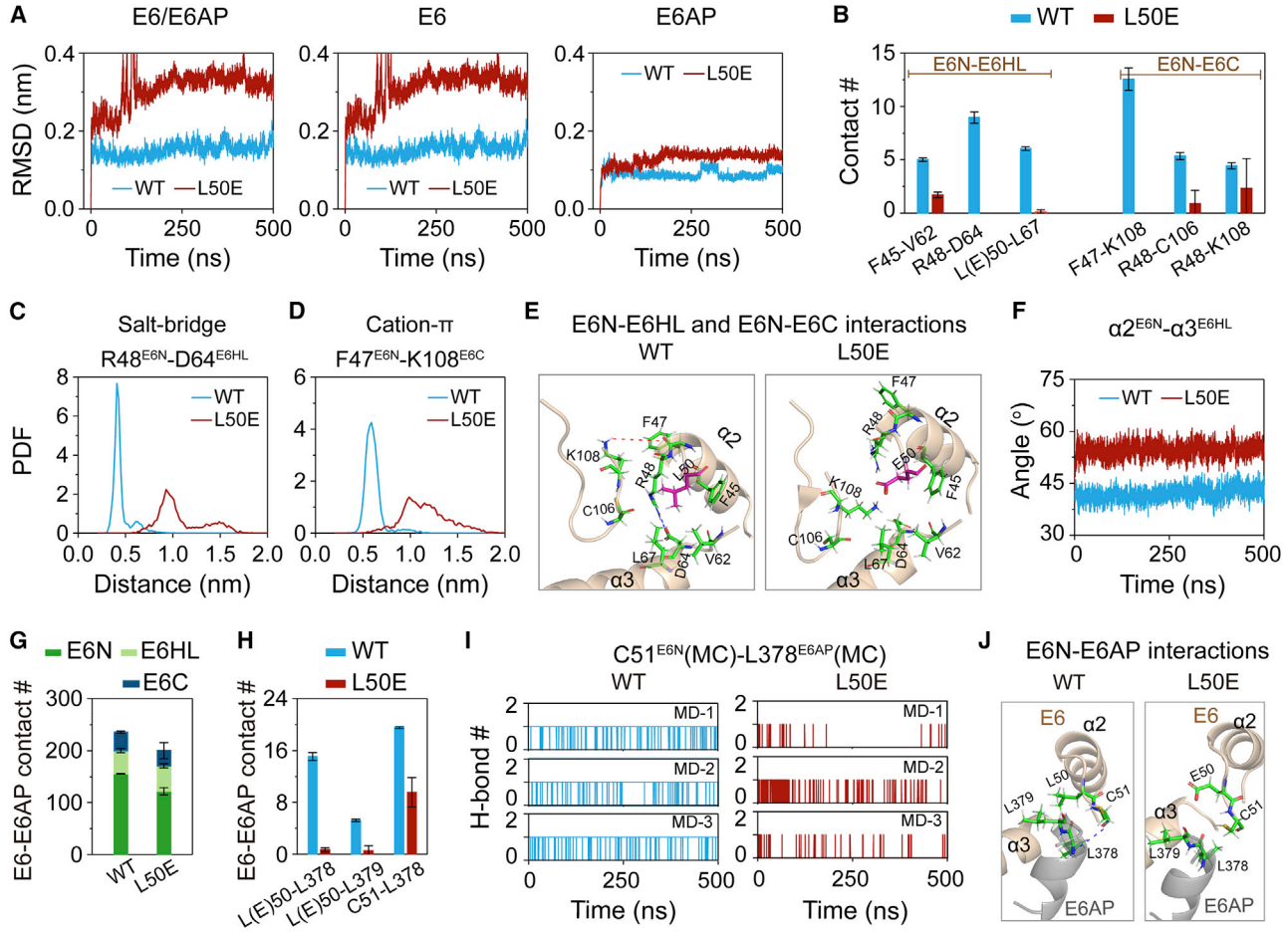

FIGURE 6 Mechanistic analyses of the inhibitory effect of L50E^{E6} mutation on E6/E6AP heterodimer formation. (*A*) The time evolution of backbone RMSD values of E6/E6AP, E6, and E6AP in heterodimers relative to their initial conformations. (*B*) Side chain contact number of E6N-E6HL and E6N-E6C. (*C*) Probability density function (PDF) of the distance of the side chain charge center of R48^{E6}-D64^{E6}. (*D*) PDF of the centroid distance between aromatic ring of F47^{E6} and ε-amino group (NH_3^+) in the side chain of K108^{E6}. (*E*) The snapshots (the center structure of the first cluster obtained by clustering analysis) showing the L50E^{E6} mutation-induced alteration of E6 interdomain interactions. Thin red dashed line: cation-π interaction; thin blue dashed line: salt bridge interaction. (*F*) The time evolution of the angle between $\alpha2^{E6N}$ and $\alpha3^{E6HL}$. (*G* and *H*) Native contact number of E6-E6AP (*g*) and of L(E)50^{E6}-L378^{E6AP}/L379^{E6AP} and C51^{E6}-L378^{E6AP} residue pairs (*H*). (*I*) The time evolution of H-bond number between the main chain atoms of C51^{E6} and L378^{E6AP}. (*J*) The snapshots (the center structure of the first cluster obtained by clustering analysis) showing the L50E^{E6} mutation-induced alteration of E6-E6AP interactions. Thick blue dashed line: H-bond. To see figure in color, go online.

E6HL can also be seen from the time evolution of the angle between $\alpha2^{E6N}$ and $\alpha3^{E6HL}$ (Figs. 6 *F* and S10 *A*), showing a drastic increase of the angle in E6^{L50E}/E6AP heterodimer (Fig. S10 *B*).

In addition, we find that the E6-E6AP binding energy in L50E^{E6} heterodimer (−45.63 kcal mol^{-1}) is significantly higher than that in WT heterodimer (−55.81 kcal mol^{-1}) (Table S6), consistent with the significant reduction of the native contact number of E6-E6AP in L50E^{E6} heterodimer (Fig. 6 *G*). These data suggest that L50E^{E6} mutation reduces the E6-E6AP binding. In more detail, L50E^{E6} mutation abolishes the hydrophobic interactions between L50^{E6} and L378^{E6AP}/L379^{E6AP} (Figs. 6 *H* and *J*), which further results in significantly decreased C51^{E6}–L378^{E6AP} H-bonding interaction. The occupancies of C51^{E6}–L378^{E6AP} H-bond in WT and L50E^{E6} heterodimer are 99% and 2%, respectively (Figs. 6 *I* and *J*). Taken together, L50E^{E6} mutation disrupts E6 interdomain interactions (F45^{E6N}-V62^{E6HL}, L50^{E6N}-L67^{E6HL}, R48^{E6N}-D64^{E6HL}, and F47^{E6N}-K108^{E6C}) and intermolecular E6N-E6AP interactions (L50^{E6}-L378^{E6AP}/L379^{E6AP}), and thus notably destabilizes E6/E6AP heterodimer. These results suggest that the aforementioned hydrophobic, salt bridge, and cation-π interactions are crucial for the heterodimer formation, and their disruption by L50E^{E6} mutation would block the binding of E6 with E6AP, thus impeding p53 recruitment.

We also explore the effect of L50E^{E6} mutation on the dynamic network of E6/E6AP heterodimer by calculating the cross correlation matrix of WT E6/E6AP and E6^{L50E}/E6AP heterodimers (Figs.7 *A* and *B*). To assess the convergence of the cross correlation values, we calculated the matrix of Cα-Cα cross correlation RMSDs using the data from

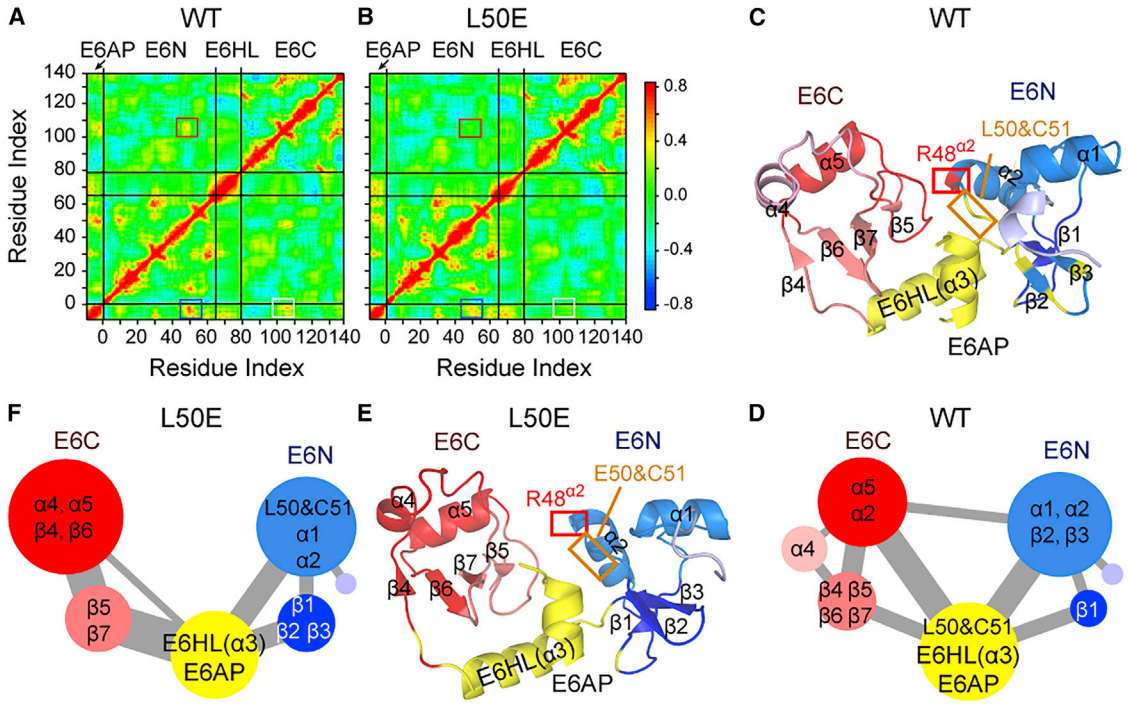

FIGURE 7 Correlation and community network analysis. The correlation matrix of (*A*) WT E6/E6AP and (*B*) $E6^{L50E}$/E6AP heterodimers. The correlation values between F47/R48/D49/L50 in E6N and C106/Q107/K108 in E6C are marked by red rectangle. The white rectangle denotes the correlation between C106/Q107/K108 in E6C and L378/L379/G380 in E6AP, and the blue rectangle denotes the correlation between L50/C51 in E6N and L378/L379/G380 in E6AP. Cartoon representation of the community network of (*C*) WT and (*E*) mutant heterodimers. Schematic diagrams of the community networks of (*D*) WT and (*F*) mutant heterodimers. In (*D*) and (*F*), each circle represents a single community. The size of the circle and the width of the edges correspond respectively to the size of community and the connectivity strength between two communities. To see figure in color, go online.

the three replicate MD simulations of WT and $L50E^{E6}$ heterodimers (Fig. S11) (56). Small differences are observed between the raw matrices of the systems (Fig. S11), suggesting the high convergence of the cross correlation values in our simulations. $L50E^{E6}$ mutation has almost no effect on all the correlation values within E6N or within E6C, whereas it reduces the correlation values between F47/R48/D49/L50 in E6N and C106/Q107/K108 in E6C (marked by red rectangle in Figs. 7 *A* and *B*). In E6 of WT heterodimer, residue R48 of E6N belongs to the red community of E6C (Figs. 7 *C* and *D*), whereas in E6 of mutant heterodimer, it belongs to the light blue community of E6N (Figs. 7 *E* and *F*). Moreover, $L50E^{E6}$ mutation results in the disappearance of the edge of E6N-E6C (Figs. 7 *D* and *F*), indicative of the significant disruption of E6N-E6C cross talk. For the cross-correlations between E6 and E6AP, two regions in the correlation matrix show significantly decreased correlation values (marked by white and blue rectangles in Figs. 7 *A* and *B*). The white rectangle denotes the correlation between C106/Q107/K108 in E6C and L378/L379/G380 in E6AP. The blue rectangle denotes the correlation between L50/C51 in E6N and L378/L379/G380 in E6AP. The community network in Figs. 7*C* and *D* shows that in WT heterodimer, $L50^{E6N}$ and $C51^{E6N}$ in the $\alpha2$-$\beta2$ loop belong to the community containing E6HL and E6AP (yellow), whereas in L50E mutant heterodimer (Figs. 7 *E* and *F*), they belong to the community containing $\alpha1$, $\alpha2$, $\beta2$, and $\beta3$ of E6N (light blue). These results demonstrate that $L50E^{E6}$ mutation disrupts the interdomain communication between E6N and E6C, the intermolecular communication between E6 and E6AP, and the global community network of E6/E6AP heterodimer.

The dissociation of the different complexes is not observed in our all-atom MD simulations. In order to explore the dissociation process, we also carried out 10-μs coarse-grained (CG) MD simulations using MARTINI force field. The CG model of E6/E6AP heterodimer, which is mapped from all-atom structure, is given in Fig. S12 *A*. It can be seen that the structure of the heterodimer collapses at the end of simulation (Figs. S12 *B* and *C*), and the dissociation of the E6/E6AP heterodimer is not observed in this MARTINI-based CG MD simulation. Therefore, a complete study of the mechanism of complex formation and how this is affected by the mutations remains to be performed using other CG models or enhanced MD simulations (such as replica exchange MD methods).

CONCLUSIONS

In summary, we have explored at an atomic-level the mechanisms of three single-site E6 mutations (F47R, R102A, and

L50E) in destabilizing the structure of E6/E6AP heterodimer and E6/E6AP/p53 heterotrimer by performing multiple MD simulations on both WT and mutant heterodimer/heterotrimer with a total simulation time of ~13 μs. We find that in heterotrimer, $F47R^{E6}$ mutation leads to an electrostatic repulsion between $R47^{E6}$ and $R290^{p53}$, and in turn it disrupts the interresidue interactions important for the stabilization of E6-p53 subinterface II and III. Specifically, E6-p53 subinterface II is mostly stabilized by hydrophobic interactions ($F47^{E6}$-$E286^{p53}$/$L289^{p53}$/$A128^{p53}$, $Y43^{E6}$-$L289^{p53}$, and $D49^{E6}$-$P128^{p53}$), salt bridge interaction ($D44^{E6}$-$R290^{p53}$), and cation-π interactions ($Y43^{E6}$/$F47^{E6}$-$R290^{p53}$). E6-p53 subinterface III is mostly stabilized by $P109^{E6}$/$P112^{E6}$-$H115^{p53}$ hydrophobic interactions and $E113^{E6}$-$T118^{p53}$ H-bonding interaction. $R102A^{E6}$ mutation abolishes the formation of interdomain H-bond between E6C and E6N ($R102(SC)^{E6C}$-$R48(MC)^{E6N}$/$D49(MC)^{E6N}$) and intermolecular H-bond between E6C and E6AP ($R102(SC)^{E6C}$-$L379(MC)^{E6AP}$, $R131(SC)^{E6C}$-$Q376(SC)^{E6AP}$), which destabilizes the structure of E6/E6AP heterodimer and thus may disfavor heterotrimer formation. Moreover, $R102A^{E6}$ mutation damages hydrophobic and cation-π interactions between F47 of E6 and E286/L298/R290 of p53, which is unfavorable for the binding of p53 with E6/E6AP heterodimer. $L50E^{E6}$ mutation severely destabilizes the structural stability of E6 by impairing interdomain interactions of E6N-E6HL ($F45^{E6N}$-$V62^{E6HL}$, $L50^{E6N}$-$L67^{E6HL}$, and $R48^{E6N}$-$D64^{E6HL}$) and E6N-E6C ($F47^{E6N}$-$K108^{E6C}$ and $R48^{E6N}$-$C106^{E6C}$/$K108^{E6C}$), which may disfavor stable heterodimer formation. In addition, $L50E^{E6}$ mutation abolishes $L50^{E6}$-$L378^{E6AP}$/$L379^{E6AP}$ hydrophobic interactions and weakens $C51^{E6}$-$L378^{E6AP}$ H-bonding interaction, thus significantly disrupts the E6/E6AP heterodimer, suggesting their key roles in the heterodimer formation. A summary of our simulation results is illustrated in a schematic diagram (Fig. S13). This study reveals the molecular interactions crucial for the binding of E6-E6AP and E6/E6AP-p53, which may provide some insights into the disruption of E6/E6AP heterodimer and E6/E6AP/p53 heterotrimer formation by the three HPV16 E6 mutations.

SUPPORTING MATERIAL

Supporting material can be found online at https://doi.org/10.1016/j.bpj.2022.03.030.

AUTHOR CONTRIBUTIONS

L.L. and G.W. conceived the project and drafted the manuscript. L.L. performed the simulations. All authors analyzed the data, reviewed, and approved the final version of the manuscript.

ACKNOWLEDGMENTS

This work has been supported by the National Key Research and Development Program of China (Grant No. 2016YFA0501702) and the National Natural Science Foundation of China (Grant No. 12074079). All simulations were performed using the GPU clusters of our group.

REFERENCES

1. Joerger, A. C., and A. R. Fersht. 2008. Structural biology of the tumor suppressor p53. *Annu. Rev. Biochem.* 77:557–582.
2. Vogelstein, B., D. Lane, and A. J. Levine. 2000. Surfing the p53 network. *Nature.* 408:307–310.
3. Olivier, M., R. Eeles, …, P. Hainaut. 2002. The IARC TP53 database: new online mutation analysis and recommendations to users. *Hum. Mutat.* 19:607–614.
4. Honda, R., H. Tanaka, and H. Yasuda. 1997. Oncoprotein MDM2 is a ubiquitin ligase E3 for tumor suppressor p53. *FEBS. Lett.* 420:25–27.
5. Lahav, G., N. Rosenfeld, …, U. Alon. 2004. Dynamics of the p53-Mdm2 feedback loop in individual cells. *Nat. Genet.* 36:147–150.
6. Thomas, M., D. Pim, and L. Banks. 1999. The role of the E6-p53 interaction in the molecular pathogenesis of HPV. *Oncogene.* 18:7690–7700.
7. Bernard, H. U., R. D. Burk, …, E.-M. de Villiers. 2010. Classification of papillomaviruses (PVs) based on 189 PV types and proposal of taxonomic amendments. *Virology.* 401:70–79.
8. Allison, D. B., and Z. Maleki. 2016. HPV-related head and neck squamous cell carcinoma: an update and review. *J. Am. Soc. Cytopathol.* 5:203–215.
9. Syrjänen, S. 2005. Human papillomavirus (HPV) in head and neck cancer. *J. Clin. Virol.* 32:59–66.
10. Marur, S., G. D'Souza, …, A. A. Forastiere. 2010. HPV-associated head and neck cancer: a virus-related cancer epidemic. *Lancet Oncol.* 11:781–789.
11. Burd, E. M. 2003. Human papillomavirus and cervical cancer. *Clin. Microbiol. Rev.* 16:1–17.
12. Monie, A., C.-F. Hung, …, T. C. Wu. 2008. Cervarix™: a vaccine for the prevention of HPV 16, 18-associated cervical cancer. *Biologics.* 2:107–113.
13. Wheeler, C. M., W. C. Hunt, …, New Mexico HPV Pap Registry Steering Committee. 2013. A population-based study of human papillomavirus genotype prevalence in the United States: baseline measures prior to mass human papillomavirus vaccination. *Int. J. Cancer.* 132:198–207.
14. Huibregtse, J. M., M. Scheffner, and P. M. Howley. 1993. Localization of the E6-AP regions that direct human papillomavirus E6 binding, association with p53, and ubiquitination of associated proteins. *Mol. Cell. Biol.* 13:4918–4927.
15. Scheffner, M., U. Nuber, and J. M. Huibregtse. 1995. Protein ubiquitination involving an E1-E2-E3 enzyme ubiquitin thioester cascade. *Nature.* 373:81–83.
16. Cooper, B., S. Schneider, …, S. V. Pol. 2003. Requirement of E6AP and the features of human papillomavirus E6 necessary to support degradation of p53. *Virology.* 306:87–99.
17. Manzo-Merino, J., M. Thomas, …, L. Banks. 2013. HPV E6 oncoprotein as a potential therapeutic target in HPV related cancers. *Expert Opin. Ther. Targets.* 17:1357–1368.
18. Ronco, L. V., A. Y. Karpova, …, P. M. Howley. 1998. Human papillomavirus 16 E6 oncoprotein binds to interferon regulatory factor-3 and inhibits its transcriptional activity. *Genes. Dev.* 12:2061–2072.
19. Zimmermann, H., R. Degenkolbe, …, M. J. O'Connor. 1999. The human papillomavirus type 16 E6 oncoprotein can down-regulate p53 activity by targeting the transcriptional coactivator CBP/p300. *J. Virol.* 73:6209–6219.
20. Kiyono, T., A. Hiraiwa, …, M. Ishibashi. 1997. Binding of high-risk human papillomavirus E6 oncoproteins to the human homologue of the Drosophila discs large tumor suppressor protein. *Proc. Natl. Acad. Sci. U S A.* 94:11612–11616.

21. Glaunsinger, B. A., S. S. Lee, …, R. Javier. 2000. Interactions of the PDZ-protein MAGI-1 with adenovirus E4-ORF1 and high-risk papillomavirus E6 oncoproteins. *Oncogene.* 19:5270–5280.

22. Thomas, M., R. Laura, …, L. Banks. 2002. Oncogenic human papillomavirus E6 proteins target the MAGI-2 and MAGI-3 proteins for degradation. *Oncogene.* 21:5088–5096.

23. Moody, C. A., and L. A. Laimins. 2010. Human papillomavirus oncoproteins: pathways to transformation. *Nat. Rev. Cancer.* 10:550–560.

24. Martinez-Zapien, D., F. X. Ruiz, …, K. Zanier. 2016. Structure of the E6/E6AP/p53 complex required for HPV-mediated degradation of p53. *Nature.* 529:541–545.

25. Zanier, K., S. Charbonnier, …, G. Travé. 2013. Structural basis for hijacking of cellular LxxLL motifs by papillomavirus E6 oncoproteins. *Science.* 339:694–698.

26. Ansari, T., N. Brimer, and S. B. V. Pol. 2012. Peptide interactions stabilize and restructure human papillomavirus type 16 E6 to interact with p53. *J. Virol.* 86:11386–11391.

27. Zanier, K., C. Stutz, …, F. Hoppe-Seyler. 2014. The E6AP binding pocket of the HPV16 E6 oncoprotein provides a docking site for a small inhibitory peptide unrelated to E6AP, indicating druggability of E6. *PloS one.* 9:e112514.

28. Malecka, K. A., D. Fera, …, R. Marmorstein. 2014. Identification and characterization of small molecule human papillomavirus E6 inhibitors. *ACS. Chem. Biol.* 9:1603–1612.

29. Ricci-López, J., A. Vidal-Limon, …, S. Aguila. 2019. Molecular modeling simulation studies reveal new potential inhibitors against HPV E6 protein. *PLoS One.* 14:e0213028.

30. Celegato, M., L. Messa, …, L. Banks. 2020. A novel small-molecule inhibitor of the human papillomavirus E6-p53 interaction that reactivates p53 function and blocks cancer cells growth. *Cancer Lett.* 470:115–125.

31. Kumar, A., E. Rathi, and S. G. Kini. 2019. Identification of E6 inhibitors employing energetically optimized structure-based pharmacophore modelling, ligand docking and molecular dynamics simulations studies. *ChemistrySelect.* 4:10701–10708.

32. Nominé, Y., M. Masson, …, E. Weiss. 2006. Structural and functional analysis of E6 oncoprotein: insights in the molecular pathways of human papillomavirus-mediated pathogenesis. *Mol. Cell.* 21:665–678.

33. Zanier, K., A. ould M'hamed ould Sidi, …, G. Travé. 2012. Solution structure analysis of the HPV16 E6 oncoprotein reveals a self-association mechanism required for E6-mediated degradation of p53. *Structure.* 20:604–617.

34. Ristriani, T., S. Fournane, …, M. Masson. 2009. A single-codon mutation converts HPV16 E6 oncoprotein into a potential tumor suppressor, which induces p53-dependent senescence of HPV-positive HeLa cervical cancer cells. *Oncogene.* 28:762–772.

35. Zhou, R., X. Huang, …, B. J. Berne. 2004. Hydrophobic collapse in multidomain protein folding. *Science.* 305:1605–1609.

36. Krone, M. G., L. Hua, …, J.-E. Shea. 2008. Role of water in mediating the assembly of Alzheimer amyloid-β Aβ16-22 protofilaments. *J. Am. Chem. Soc.* 130:11066–11072.

37. Lei, J., G. Sheng, …, X. Huang. 2019. Two symmetric arginine residues play distinct roles in Thermus thermophilus Argonaute DNA guide strand-mediated DNA target cleavage. *Proc. Natl. Acad. Sci. U S A.* 116:845–853.

38. Wassman, C. D., R. Baronio, …, G. W. Hatfield. 2013. Computational identification of a transiently open L1/S3 pocket for reactivation of mutant p53. *Nat. Commun.* 4:1–9.

39. Ng, J. W., D. Lama, …, A. Y. Sim. 2015. R248Q mutation—beyond p53-DNA binding. *Proteins.* 83:2240–2250.

40. Pradhan, M. R., J. W. Siau, …, C. S. Verma. 2019. Simulations of mutant p53 DNA binding domains reveal a novel druggable pocket. *Nucleic Acids Res.* 47:1637–1652.

41. Li, L., X. Li, …, G. Wei. 2020. Common cancer mutations R175H and R273H drive the p53 DNA-binding domain towards aggregation-prone conformations. *Phys. Chem. Chem. Phys.* 22:9225–9232.

42. Lei, J., R. Qi, …, B. Ma. 2019. Conformational stability and dynamics of the cancer-associated isoform Δ133p53β are modulated by p53 peptides and p53-specific DNA. *FASEB. J.* 33:4225–4235.

43. Ma, B., Y. Pan, …, R. Nussinov. 2005. Comparison of the protein-protein interfaces in the p53-DNA crystal structures: towards elucidation of the biological interface. *Proc. Natl. Acad. Sci. U S A.* 102:3988–3993.

44. ElSawy, K. M., D. P. Lane, …, L. S. Caves. 2016. Recognition dynamics of p53 and MDM2: implications for peptide design. *J. Phys. Chem. B.* 120:320–328.

45. Liu, S.-X., Y.-Z. Geng, and S.-W. Yan. 2017. Structural effects and competition mechanisms targeting the interactions between p53 and MDM2 for cancer therapy. *Front. Phys.* 12:128908.

46. Lima, I., A. Navalkar, …, E. A. Cino. 2020. Biophysical characterization of p53 core domain aggregates. *Biochem. J.* 477:111–120.

47. Lei, J., R. Qi, …, B. Ma. 2016. Self-aggregation and coaggregation of the p53 core fragment with its aggregation gatekeeper variant. *Phys. Chem. Chem. Phys.* 18:8098–8107.

48. Bauer, M. R., A. Krämer, …, A. C. Joerger. 2020. Targeting cavity-creating p53 cancer mutations with small-molecule stabilizers: the Y220X paradigm. *ACS. Chem. Biol.* 15:657–668.

49. The PyMOL Molecular Graphics System, Version 2.0. Schrödinger, LLC.

50. Van Der Spoel, D., E. Lindahl, …, H. J. Berendsen. 2005. GROMACS: fast, flexible, and free. *J. Comput. Chem.* 26:1701–1718.

51. Huang, J., S. Rauscher, …, A. D. MacKerell. 2017. CHARMM36m: an improved force field for folded and intrinsically disordered proteins. *Nat. Methods.* 14:71–73.

52. Lu, Q., Y.-H. Tan, and R. Luo. 2007. Molecular dynamics simulations of p53 DNA-binding domain. *J. Phys. Chem. B.* 111:11538–11545.

53. Nosé, S., and M. Klein. 1983. Constant pressure molecular dynamics for molecular systems. *Mol. Phys.* 50:1055–1076.

54. Bussi, G., D. Donadio, and M. Parrinello. 2007. Canonical sampling through velocity rescaling. *J. Chem. Phys.* 126:014101.

55. Deserno, M., and C. Holm. 1998. How to mesh up Ewald sums. I. A theoretical and numerical comparison of various particle mesh routines. *J. Chem. Phys.* 109:7678–7693.

56. Hernandez Gonzalez, J. E., L. Hernández Alvarez, …, V. B. Leite. 2019. Prediction of noncompetitive inhibitor binding mode reveals promising site for allosteric modulation of Falcipain-2. *J. Phys. Chem. B.* 123:7327–7342.

Biophysical Journal, Volume *121*

Supplemental information

Deciphering the mechanisms of HPV E6 mutations in the destabilization of E6/E6AP/p53 complex

Le Li, Xuewei Dong, Yiming Tang, Zenghui Lao, Xuhua Li, Jiangtao Lei, and Guanghong Wei

Supporting Information

Deciphering the mechanisms of HPV E6 mutations in the destabilization of E6/E6AP/p53 complex

Le Li[a], Xuewei Dong[a], Yiming Tang[a], Zenghui Lao[a], Xuhua Li[b], Jiangtao Lei[c] and Guanghong Wei[a]*

a. Department of Physics, State Key Laboratory of Surface Physics, and Key Laboratory for Computational Physical Sciences (Ministry of Education), Fudan University, Shanghai 200438, People's Republic of China.

b. MOE Key Laboratory for Nonequilibrium Synthesis and Modulation of Condensed Matter, School of Physics, Xi'an Jiaotong University, Xi'an 710049, China

c. Institute of Space Science and Technology, Nanchang University, Xuefu Avenue 999, Nanchang City 330031, China.

This supporting material contains analysis methods, six supplemental tables (Tables S1-S6), thirteen supplemental figures (Figures S1-S13) and references.

Analysis methods

Conformational property analysis. We utilized the tools implemented in the GROMACS software package and in-house codes to analyze our trajectory data. The following several parameters are used to examine the influences of the E6 mutations on the structure stabilities of the heterodimer and the heterotrimer: backbone root mean square derivation (RMSD), hydrogen bond (H-bond) number, contact number and distance distributions of residue pairs with the ability to form salt-bridge and cation-π interactions. Here, an H-bond is considered to be formed if the distance between the donor atom D and the acceptor atom A is ≤ 0.35 nm and the D-H···A angle is $\geq 150°$. An atomic contact is considered if the distance between two carbon atoms of nonsequential residues lies within 0.54 nm or the distance between any other two atoms of nonsequential residues comes within 0.46 nm. We first calculated the charge center of the charged group of the four residues: Arg^+, Lys^+, Glu^- and Asp^-, and then calculated the distance of the charge center between two oppositely charged residues. A salt-bridge is formed if the charge center distance is within 0.40 nm(1). A cation-π interaction is considered when the minimum distance between the centroid of aromatic ring and the ε-amino group (NH_3^+) in the side chain of residue Lysine or residue Argine becomes around 0.6 nm(2, 3). We also calculated the binding free energy with the

molecular mechanics/linear Generalized Born surface area (MM/GBSA) method using MMPBSA.py program of Ambertool(4, 5). The binding free energy ($\Delta G_{binding}$) between a ligand and a receptor is calculated as: $\Delta G_{binding} = \Delta E_{vdW} + \Delta E_{elec} + \Delta G_{polar} + \Delta G_{nonpolar}$. Here, E_{vdW} and E_{elec} are, respectively, the van der Waals (vdW) and the electrostatic interaction energies in vacuum. The $G_{polar} + G_{nonpolar}$ is the solvation free energy that is required to transfer a solute from vacuum into the solvent, where $G_{polar}$and $G_{nonpolar}$ are the electrostatic and non-electrostatic contributions to the solvation free energy, respectively. G_{polar} is calculated using the GB implicit solvent model (igb = 1) with a salt concentration of 0.1 M and $G_{nonpolar}$ is estimated using the solvent accessible surface area (SASA).

Community network analysis. Dynamic network analysis was performed using 'gmx covar' tool and our in-house codes. The Cα atom of an amino acid residue is considered as a node of the community network. The covariance value of two nodes was calculated using 'gmx covar' tool implemented in the GROMACS package. Then, the dynamic cross-correlation between two nodes was calculated as:

$$C_{ij} = \frac{Cov(i,\ j)}{\sqrt{Var(i) \cdot Var(j)}} = \frac{< (\vec{r}_i(t) - < \vec{r}_i(t) >) \cdot (\vec{r}_j(t) - < \vec{r}_j(t) >) >}{\sqrt{(< \vec{r}_i(t)^2 > - < \vec{r}_i(t) >^2) \cdot (< \vec{r}_j(t)^2 > - < \vec{r}_j(t) >^2)}}$$

where C_{ij} stands for the dynamic cross-correlation of two nodes (i and j) and Cov(i, j) is the covariance of the two nodes. Var(i) and Var(j) are the variance of node i and j, respectively. The cross-correlation values are zeroed and the corresponding edges are thus removed when the contact probabilities of corresponding residue pairs are less 0.7, in accordance with a number of previous studies(6-9). An atomic contact is taken to be formed using the criteria defined above. The weight of each edge is defined as $-\ln|C_{ij}|$. On the basis of the dynamic network, the shortest path (or the optimal path) between two residues can be obtained using codes developed by *Eargle* and *Sethi*(6). The betweenness of each edge is defined as the number of shortest paths that pass through that edge. The optimal community distribution is calculated using the Girvan-Newman algorithm(10), which iteratively removes the edge with the highest betweenness and recalculates the betweenness of all remaining edges until the modularity of the community network is maximized. The modularity is a measure of the quality of a particular division of a network, and the bigger the modularity, the better the division quality(11). The community analysis was conducted for each replicate trajectory and the results of all independent analysis were averaged. Community network analysis has been used to study the conformational dynamics of proteins(12-14).

As the terminal residues of E6AP (C-terminal residues 382-383), p53C (N-terminal residues 94-95 and C-terminal residues 291-292) and E6 (N-terminal residues 1-3 and C-terminal residues 140-143) have relatively high flexibility, they are excluded in all the analysis. Unless specified, we used the last 200 ns data of E6/E6AP heterodimers and the last 300 ns data of E6/E6AP/p53 heterotrimers for analysis.

Table S1. The binding free energy (kcal mol^{-1}) between E6 and E6AP in WT and F47R^{E6} heterodimers.

System	ΔE_{vdW}	ΔE_{elec}	ΔG_{polar}	$\Delta G_{nonpolar}$	$\Delta G_{binding}$
WT dimer	-50.49 ± 2.06	-666.17 ± 23.58	669.31 ± 24.63	-8.46 ± 0.35	-55.81 ± 1.42
F47R^{E6} dimer	-49.32 ± 0.35	-707.76 ± 14.08	710.17 ± 15.71	-8.64 ± 0.06	-55.55 ± 1.87

Table S2. The binding free energy (kcal mol^{-1}) between E6 and p53 in WT and F47R^{E6} heterotrimers.

System	ΔE_{vdW}	ΔE_{elec}	ΔG_{polar}	$\Delta G_{nonpolar}$	$\Delta G_{binding}$
WT trimer	-55.63 ± 4.35	-92.59 ± 6.60	116.19 ± 3.71	-11.09 ± 0.58	-43.13 ± 1.87
F47R^{E6} trimer	-50.79 ± 8.69	-65.32 ± 20.69	96.52 ± 21.74	-9.72 ± 1.43	-29.31 ± 11.24

Table S3. The binding free energy (kcal mol^{-1}) between E6 and E6AP in WT and R102A^{E6} heterodimers.

System	ΔE_{vdW}	ΔE_{elec}	ΔG_{polar}	$\Delta G_{nonpolar}$	$\Delta G_{binding}$
WT dimer	-50.49 ± 2.06	-666.17 ± 23.58	669.31 ± 24.63	-8.46 ± 0.35	-55.81 ± 1.42
R102A^{E6} dimer	-54.52 ± 3.05	-557.06 ± 48.58	563.61 ± 46.69	-8.99 ± 0.44	-56.95 ± 5.38

Table S4. The binding free energy (kcal mol^{-1}) between E6 and E6AP in the three MD runs of R102A^{E6} heterodimer.

R102A heterodimer					
MD run	ΔE_{vdW}^{WT}	ΔE_{elec}^{WT}	ΔG_{polar}^{WT}	$\Delta G_{nonpolar}^{WT}$	$\Delta G_{binding}^{WT}$
MD-1	-51.66	-521.69	527.91	-8.57	-54.01
MD-2	-54.17	-537.03	546.48	-8.96	-53.69
MD-3	-57.73	-613.45	616.45	-9.442	-61.16

Table S5. The binding free energy (kcal mol^{-1}) between E6 and p53 in WT and R102A^{E6} heterotrimers.

System	ΔE_{vdW}	ΔE_{elec}	ΔG_{polar}	$\Delta G_{nonpolar}$	$\Delta G_{binding}$
WT trimer	-55.63 ± 4.35	-92.59 ± 6.60	116.19 ± 3.71	-11.09 ± 0.58	-43.13 ± 1.87
R102A^{E6} trimer	-57.19 ± 5.88	-117.05 ± 18.12	145.21 ± 13.94	-11.13 ± 0.48	-40.17 ±11.37

Table S6. The binding free energy (kcal mol^{-1}) between E6 and E6AP in WT and L50E^{E6} heterodimers.

System	ΔE_{vdW}	ΔE_{elec}	ΔG_{polar}	$\Delta G_{nonpolar}$	$\Delta G_{binding}$
WT dimer	-50.49 ± 2.06	-666.17 ± 23.58	669.31 ± 24.63	-8.46 ± 0.35	-55.81 ± 1.42
L50E^{E6} dimer	-49.12 ± 6.60	-541.91 ± 39.97	554.01 ± 40.52	-8.62 ± 0.78	-45.63 ± 6.65

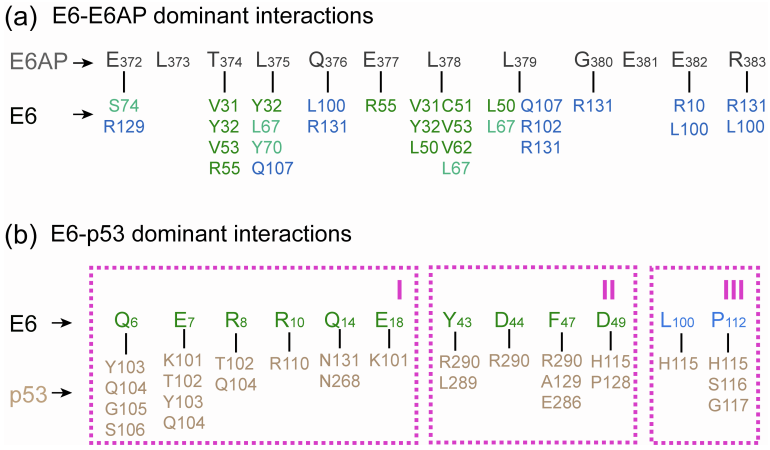

Figure S1. (a) The key interactions between E6 and E6AP in X-ray crystal structure(15). (b) The key interactions between E6 and p53 in X-ray crystal structure(16). Wheat: p53; green: E6N; cyan: E6HL; blue: E6C; gray: LxxLL motif of E6AP.

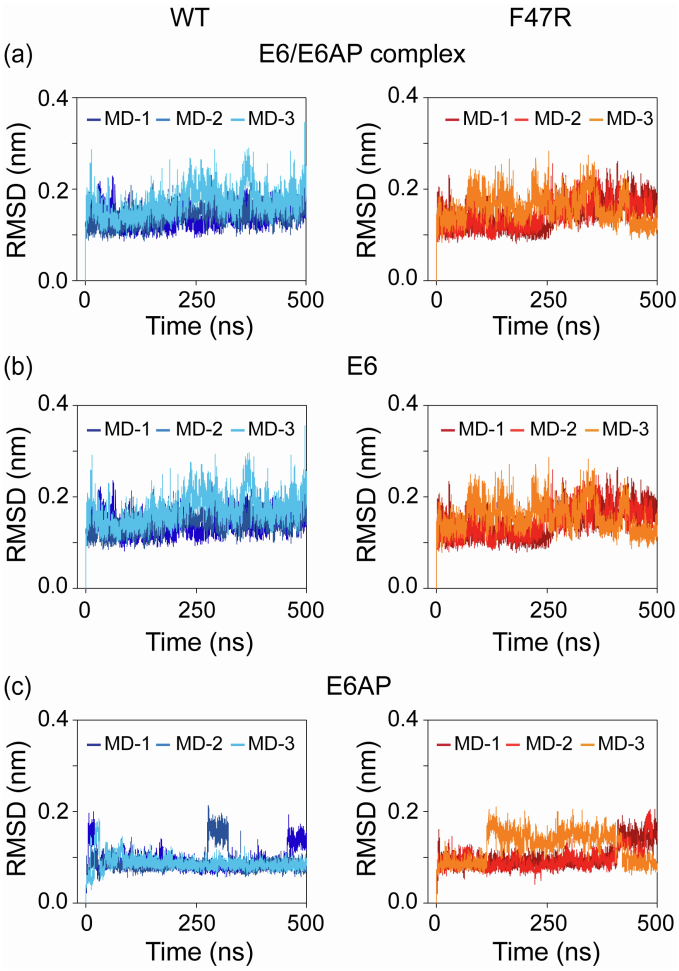

Figure S2. The time evolution of backbone root mean square deviation (RMSD) values of (a) E6/E6AP, (b) E6 and (c) E6AP relative to their initial conformations in WT and F47R mutant E6/E6AP heterodimers.

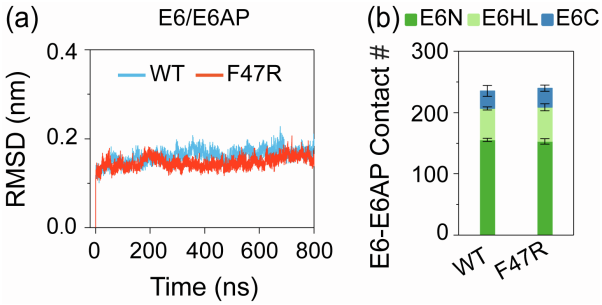

Figure S3. (a) The time evolution of backbone RMSD values of E6/E6AP relative to its initial conformations in WT and F47R mutant E6/E6AP/p53 heterotrimers. (b) The number of native contacts between E6 and E6AP in WT and F47R mutant E6/E6AP/p53 heterotrimers. The data are averaged over three independent MD runs.

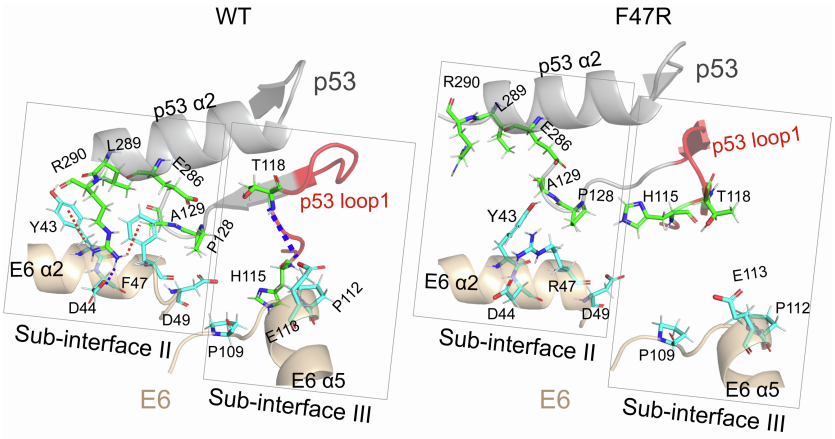

Figure S4. The snapshots (from the center structure of the first cluster) showing the F47R^{E6} mutation-induced alteration of E6-p53 interactions. Thin red dashed line: cation-π interaction; thin blue dashed line: salt-bridge interaction; thick blue dashed line: H-bond.

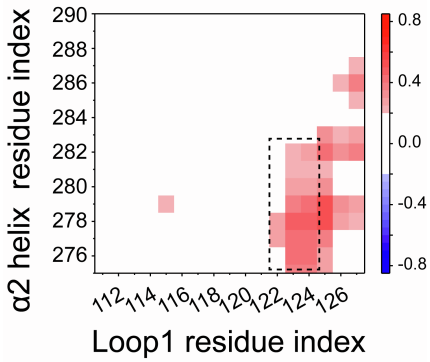

Figure S5. The correlation matrix between α2-helix^{p53} and loop1^{p53} in E6^{F47R}/E6AP/p53 heterotrimer. For clarity, correlations whose absolute value is less than 0.2 are not shown.

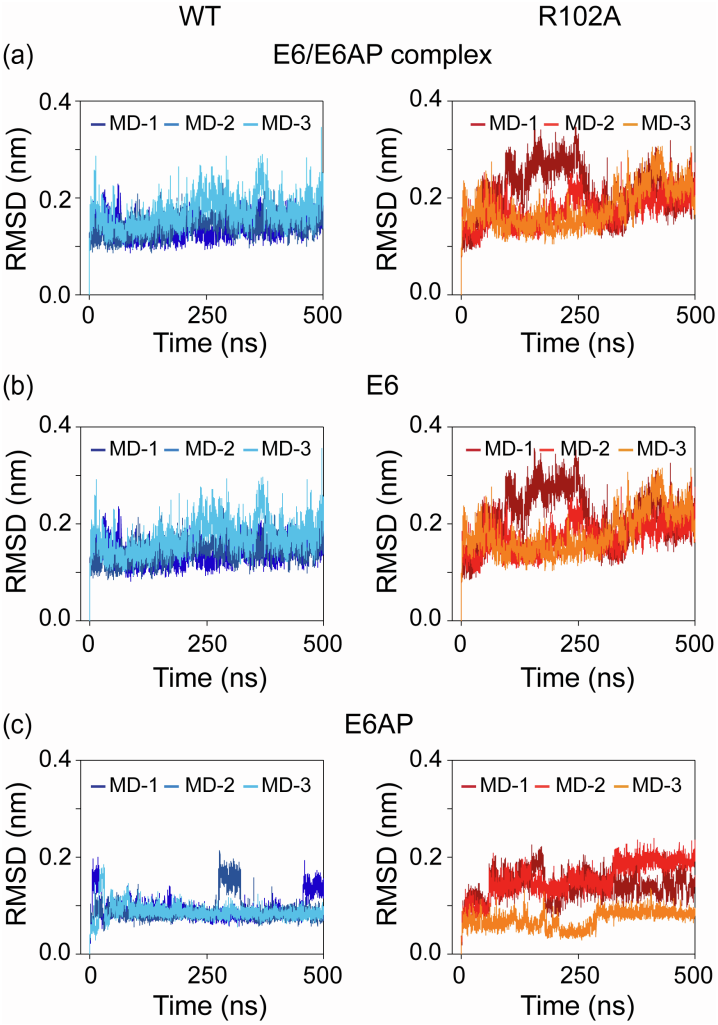

Figure S6. The time evolution of backbone RMSD values of (a) E6/E6AP, (b) E6 and (c) E6AP relative to their initial conformations in WT and R102A mutant E6/E6AP heterodimers.

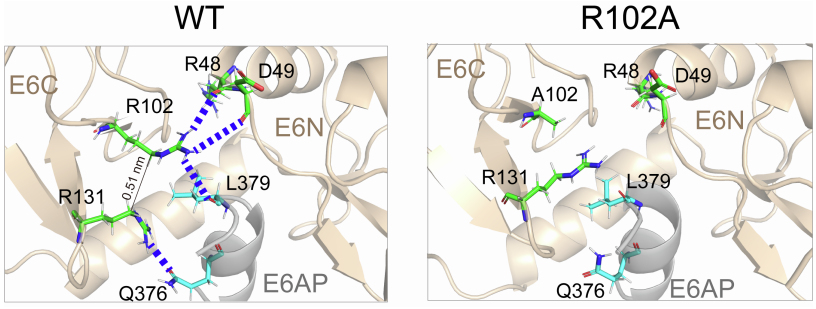

Figure S7. The snapshots (from the center structure of the first cluster of the clustering analysis) showing the R102A^{E6} mutation-induced alteration of E6C-E6N and E6C-E6AP interactions. Thick blue dashed line: H-bond.

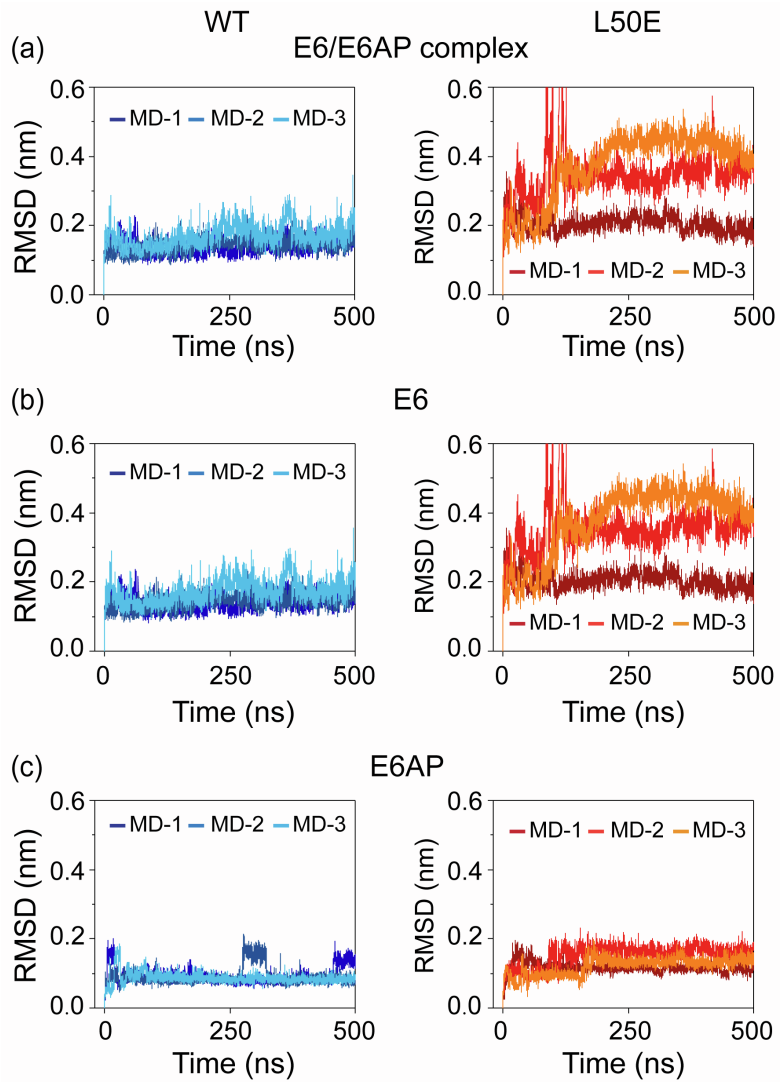

Figure S8. The time evolution of backbone RMSD values of (a) E6/E6AP, (b) E6 and (c) E6AP relative to their initial conformations in WT and L50E mutant E6/E6AP heterodimers.

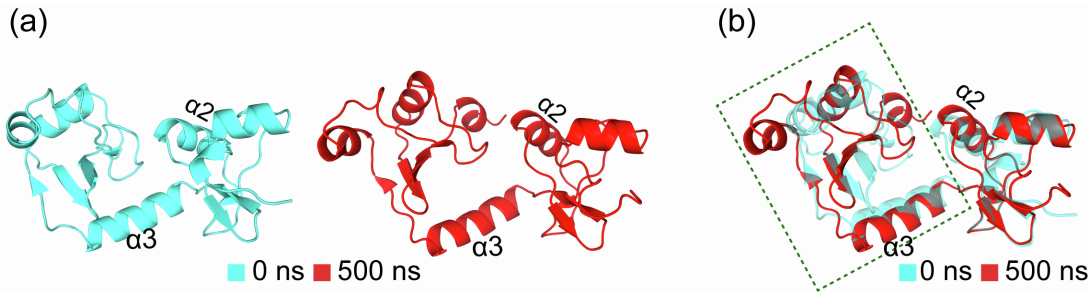

Figure S9. (a) The initial and final conformations of E6 in $E6^{L50E}$/E6AP heterodimer. (b) The final conformation of $E6^{L50E}$ superposed with its initial conformation.

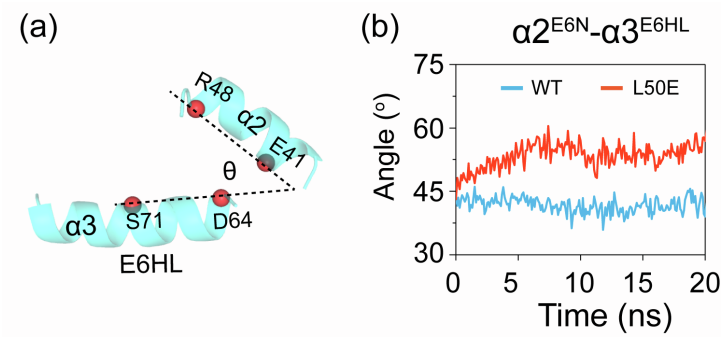

Figure S10. (a) A snapshot showing the angle between α2-helix^{E6N} and α3-helix^{E6HL}. (b) The time evolution of the angle within the first 20 ns simulation time.

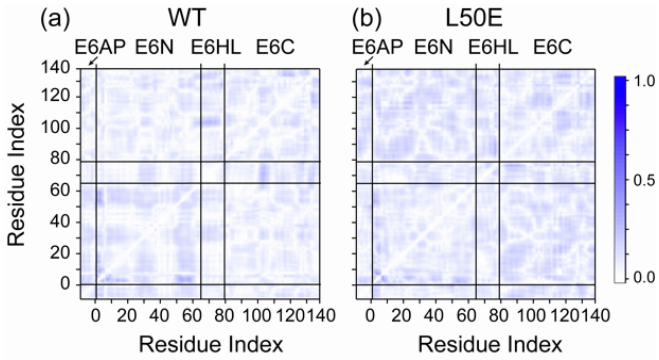

Figure S11. The matrix of Cα-Cα cross-correlation RMSDs of (a) WT and (b) L50E^{E6} heterodimers. Cα-Cα cross-correlation RMSD values were calculated using the data from the three replicate MD simulation of each system.

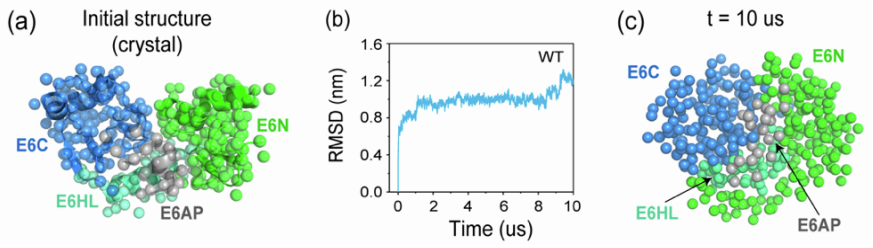

Figure S12. Analysis of simulation results obtained using coarse-grained MARTINI force field for WT E6/E6AP dimer. (a) The snapshot of initial coarse-grained model. (b) Time evolution of RMSD of the heterodimer relative to its initial conformation. (c) The snapshot of heterodimer at t = 10 μs.

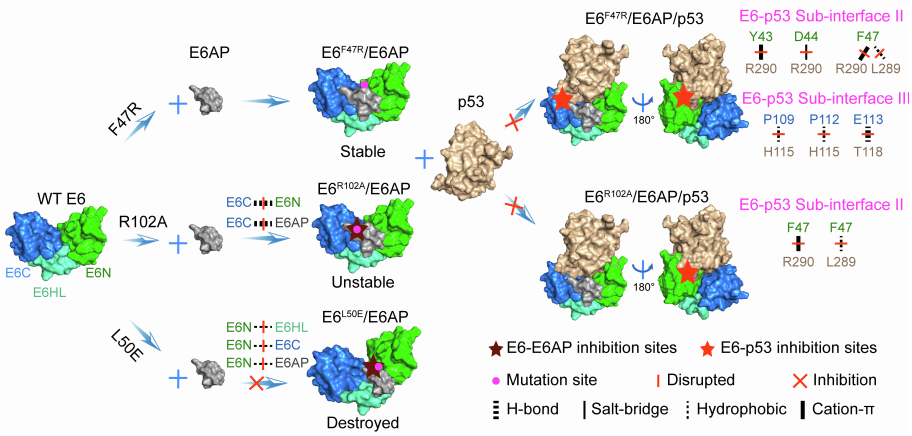

Figure S13. The schematic diagram showing how each p53-degradation-defective HPV16 E6 mutant disrupts the formation of E6/E6AP heterodimer and E6/E6AP/p53 heterotrimer.

References

1. Li, L., X. Li, Y. Tang, Z. Lao, J. Lei, and G. Wei. 2020. Common cancer mutations R175H and R273H drive the p53 DNA-binding domain towards aggregation-prone conformations. *Phys. Chem. Chem. Phys.* 22:9225-9232.
2. Ma, J. C., and D. A. Dougherty. 1997. The cation-π interaction. *Chem. Rev.* 97:1303-1324.
3. Gallivan, J. P., and D. A. Dougherty. 1999. Cation-π interactions in structural biology. *Proc. Natl. Acad. Sci. U. S. A.* 96:9459-9464.
4. Rastelli, G., A. D. Rio, G. Degliesposti, and M. Sgobba. 2010. Fast and accurate predictions of binding free energies using MM-PBSA and MM-GBSA. *J. Comput. Chem.* 31:797-810.
5. Miller III, B. R., T. D. McGee Jr, J. M. Swails, N. Homeyer, H. Gohlke, and A. E. Roitberg. 2012. MMPBSA. py: an efficient program for end-state free energy calculations. *J. Chem. Theory. Comput.* 8:3314-3321.
6. Sethi, A., J. Eargle, A. A. Black, and Z. Luthey-Schulten. 2009. Dynamical networks in tRNA:protein complexes. *Proc. Natl. Acad. Sci. U. S. A.* 106:6620-6625.
7. Zhao, Y., Y. Jian, Z. Liu, H. Liu, Q. Liu, C. Chen, Z. Li, L. Wang, H. H. Huang, and C. Zeng. 2017. Network analysis reveals the recognition mechanism for dimer formation of bulb-type lectins. *Sci. Rep.* 7:1-9.
8. Contreras-Riquelme, S., J.-A. Garate, T. Perez-Acle, and A. J. Martin. 2018. RIP-MD: a tool to study residue interaction networks in protein molecular dynamics. *PeerJ.* 6:e5998.
9. Tang, Y., Y. Yao, and G. Wei. 2021. Unraveling the Allosteric Mechanism of Four Cancer-related Mutations in the Disruption of p53-DNA Interaction. *J. Phys. Chem. B.* 125:10138-10148
10. Girvan, M., and M. E. Newman. 2002. Community structure in social and biological networks. *Proc. Natl. Acad. Sci. U. S. A.* 99:7821-7826.
11. Newman, M. E., and M. Girvan. 2004. Finding and evaluating community structure in networks. *Phys. Rev. E.* 69:026113.
12. Qian, H., Y. Zou, Y. Tang, Y. Gong, Z. Qian, G. Wei, and Q. Zhang. 2018. Proline hydroxylation at different sites in hypoxia-inducible factor 1α modulates its interactions with the von Hippel-Lindau tumor suppressor protein. *Phys. Chem. Chem. Phys.* 20:18756-18765.
13. Lei, J., R. Qi, Y. Tang, W. Wang, G. Wei, R. Nussinov, and B. Ma. 2019. Conformational stability and dynamics of the cancer-associated isoform Δ133p53β are modulated by p53 peptides and p53-specific DNA. *FASEB. J.* 33:4225-4235.
14. Tang, Y., Y. Yao, and G. Wei. 2020. Structural and dynamical mechanisms of a naturally occurring variant of the human prion protein in preventing prion conversion. *Chinese. Phys. B.* 29:108710.
15. Zanier, K., S. Charbonnier, A. O. M. h. O. Sidi, A. G. McEwen, M. G. Ferrario, P. Poussin-Courmontagne, V. Cura, N. Brimer, K. O. Babah, T. Ansari, , I. Muller, R. H. Stote, J. Cavarelli, S. V. Pol, and G. Travé. 2013. Structural basis for hijacking of cellular LxxLL motifs by papillomavirus E6 oncoproteins. *Science.* 339:694-698.
16. Martinez-Zapien, D., F. X. Ruiz, J. Poirson, A. Mitschler, J. Ramirez, A. Forster, A. Cousido-Siah, M. Masson, S. V. Pol, A. Podjarny, G. Travé, and K. Zanier. 2016. Structure of the E6/E6AP/p53 complex required for HPV-mediated degradation of p53. *Nature.* 529:541-545.